Research Square

Preprints are preliminary reports that have not undergone peer review.
They should not be considered conclusive, used to inform clinical practice,
or referenced by the media as validated information.

Development of a Modified Shearing Cooling Roll System for Semi-Solid Processing of A356 Aluminium Alloy towards Refined Microstructure and Enhanced Mechanical Properties

Ruchika Dhyani
Prashant Tadge
Balaji Chandrakanth
Harsh Bhakta
Adwaita Maity
Himadri Roy
Dipankar Chatterjee
Sudip Samanta

sudip.cmeri@csir.res.in

CMERI: Central Mechanical Engineering Research Institute CSIR

Research Article

Keywords: Shearing Cooling Roll (SCR), Semi-solid processing, A356 aluminium alloy, Microstructural refinement, Mechanical properties

Posted Date: May 6th, 2026

DOI: https://doi.org/10.21203/rs.3.rs-8668463/v1

License: This work is licensed under a Creative Commons Attribution 4.0 International License.
Read Full License

Abstract

This study focuses on Shearing Cooling Roll (SCR), a semi-solid processing technique that synergizes rheocasting and forming to refine microstructures and enhance mechanical properties in A356 aluminium (Al) alloy. The developed laboratory-scale SCR setup, designed for semi-solid processing of alloys, employs a rotational roll and a stationary shoe forming a cavity with an adjustable gap to impose controlled shear and efficient cooling during solidification. This thermo-mechanical combination fragments dendritic *α*-Al into spheroidal grains and refines the eutectic Si from coarse platelets to uniformly distributed particles. The test parameters of the developed setup were varied by adjusting the roll speed and the gap between the roll and the stationary shoe. At an optimal condition of 120 RPM roll speed and a 6 mm roll-shoe gap, the SCR process achieves a UTS of 330 MPa with 11.6% elongation, demonstrating a significant improvement over conventional casting and rheocasting routes, while achieving comparable performance to thixoforming process. Finite Element Analysis (FEA) corroborates SCR's thermo-mechanical efficacy, revealing peak shear stress and strain at the billet-roll interface, which drives dynamic recrystallization and pore minimization. T6 heat treatment further dissolves Si platelets and precipitates nanoscale β" dispersoids, while fractography confirms a ductile dimpled rupture mechanism, contrasting with brittle Si-dominated failure in conventional casting. This work establishes SCR as a paradigm shift in semi-solid processing of aluminium alloys, merging microstructure control, defect suppression, and sustainability within a single-step forming operation.

1. Introduction

Semi-solid metal processing (SSMP) is a significant advancement in foundry, offering improved mechanical properties, reduced porosity, and better dimensional accuracy compared to traditional casting technique [1, 2]. SSMP incorporates the thixotropic properties of metals to regulate microstructural evolution, producing components with remarkable strength, elongation, and fatigue resistance [3, 4, 5]. Processing metals or alloys in semi-solid state often results in reduced cycle times, minimizes thermal stresses on molds, extends tool life, and offers economic and environmental benefits, such as low-cost feedstock, recyclability, and reduced waste [2, 5]. A key factor in semi-solid processing of metal and alloys is the preparation of slurries with non-dendritic microstructures, promoting thixotropic flow during forming [6, 7, 8]. Such dendritic morphologies typically formed in conventional casting and solidification methods, are prone to porosity and brittleness. Porosities are commonly observed in cast products, and the fracture path preferentially follows regions with localized and clustered pores which, severely restrict tensile deformation and result in reduced elongation and lower ultimate tensile strength [9]. Processing in the semi-solid state disrupts dendritic growth through shear-induced fragmentation and spheroidization, while also reducing porosity compared to gravity castings [10, 11, 12]. Various techniques exist for generating non-dendritic structures, including both shearing and non-shearing methods. Non-shearing techniques comprise non-agitation liquid routes such as spray casting, chemical grain refining, liquidus casting (NRC), the direct thermal method (DTM), the gas-induced semisolid process (GISS), and ultrasonic vibrations, as well as solid-state routes such as SIMA, RAP, DPRM, and solid-solution treatment with partial remelting [6, 8]. These techniques produce non-

dendritic microstructures through controlled solidification conditions, chemical additives, or thermal and deformation treatments. Conversely, mechanical stirring [13], Magneto-Hydro-Dynamic (MHD) stirring/Electro-Magnetic Stirring (EMS) [14], electromagnetic and ultrasonic stirring [15]; Swirled Enthalpy Equilibration Device (SEED); twin-screw rheocasting; and cooling-slope casting [11, 12] apply shear during solidification, leading to fragmentation of dendritic arms. The evolution of spheroidal or globular microstructures is governed by mechanisms such as nucleation and grain growth followed by dendrite fragmentation [16], the establishment of equiaxed grains, and their subsequent spheroidization and diffusion-controlled coarsening [17]. Cooling Slope casting process promises to be a simple yet useful technique to produce semi-solid feedstock for rheo pressure die casting and thixoforming processes. Kumar *et al.* [12] reported that cooling-slope casting promotes grain refinement in aluminium alloys. Rheocasting and T6 heat treatment of A356 results in 241 MPa YS, 310 MPa UTS, with 18%elongation. Increasing the angle from 30° to 45° reduced α-Al size from 71 μm to 65 μm and improved shape factor from 1.8 to 1.4. Haga & Kapranos [18] studied two simple rheocasting processes and found that cooling-slope casting offers superior mechanical performance compared to conventional thixoforming, producing 310 MPa UTS, 241 MPa YS, and 18% elongation. In contrast, low-superheat casting exhibits slightly lower values of 290 MPa UTS, 237 MPa YS, and 12% elongation. Birol [19] also evaluated the effect of cooling-slope (CS) casting and thixoforming on A390 al alloy. CS casting produces dispersed primary Si particles in an Al–Si eutectic matrix, along with some intermetallic phases. The refined CS-cast feedstock leads to higher hardness (90 ± 4 HB) after thixoforming compared to conventional die-cast material (80 ± 12 HB). Artificial ageing (T5) increases the hardness of the thixoformed alloy to 101 ± 8 HB, while full solutionizing followed by ageing (T6) results in a much higher hardness of 144 ± 3 HB. Das et al. [20], investigated the cooling-slope technique for A356 alloy and demonstrated that it leads to significant grain refinement along with the formation of a near-spherical primary α-Al morphology, with grain diameters on the order of ~ 30–35 μm and sphericity values approximately in the range of 0.80–0.85. As a result, the cooling-slope processed alloy exhibits improved properties of approximately 155 MPa UTS and 9% elongation, compared to 145 MPa UTS and 7.5% elongation in material processed without grain refinement. In contrast, direct pouring yields substantially inferior values of 125 MPa UTS and 3.5% elongation. Evidence in the literature indicates that cooling-slope processing improves mechanical properties, reduces segregation and porosity as compared to conventional casting. It significantly lowers cost owing to simple equipment and ease of temperature control, while effectively producing refined grains and an equiaxed α-Al phase. However, it remains susceptible to pores, oxides, and solidification-shell formation, which reduce microstructural uniformity. These limitations are addressed by subsequent thixoforming, which reduces porosity, increases dislocation density, and promotes microstructural homogeneity owing to applied pressure in forming feedstock processed by cooling-slope subjected to thixoforming, attains 234 MPa yield strength, 293 MPa ultimate tensile strength, and 15% elongation[12]. Tahamtan *et al.* [7] compared gravity casting, rheocasting, and Thixoforming for A356 alloy and discussed about porosity levels as well as tensile properties. After T6 treatment, rheocast A356 alloy shows superior mechanical properties compared to gravity-cast material, achieving UTS of 212 ± 7.40 MPa and 4.7% elongation in contrast to only 137 ± 12.00 MPa UTS and 2.9% elongation for gravity cast. Thixo-formed A356 processed at 590°C reached

378 ± 10.30 MPa UTS and 24.5% elongation, again outperforming rheocast alloys. The improvement is due to significantly lower porosity; without T6, gravity-cast samples contain 12.4%±1.2 porosity compared to 2.1%±0.2 for rheocast; after T6, porosity drops to 9.8%±1.1 and 1.7%±0.3, respectively. Thixoformed samples exhibit a porosity level of only 0.21%, which is significantly lower than that of rheocast and gravity-cast samples. Similarly, Jin [11] investigated the rheocasting, upsetting, and thixoforming processes for A356 and Al6061 alloys. The equivalent diameter of the primary α-Al grains decreased from approximately 80 μm in the rheocast condition to about 65 μm after final forming, while the shape factor improved from 1.61 to around 1.23, indicating a transition toward a more globular morphology. Correspondingly, the tensile strength increased from 205 MPa to 265 MPa, whereas the elongation decreased from 9.8% to 6.9%. This behavior is attributed to grain refinement and enhanced particle sphericity, which improve strength but reduce ductility due to limited deformation capability of the refined microstructure. Yang *et al.* [9] reported that the presence of casting pores reduces the ultimate tensile strength (UTS) of A356-T6 alloy to 258 MPa, about 8% lower than the 279 MPa observed in pore-free specimens due to the reduced effective load-bearing area. Elongation is more severely affected, decreasing to 4.5% in porous samples compared to 8% in coarse and 14.6% in fine pore-free microstructures. This significant loss in ductility is attributed to stress concentration at pore edges, which promotes early microcrack initiation and premature fracture. Thixoforming surpasses rheocast and gravity-cast methods by lowering porosity and Si-particle aspect ratio, yielding greater strength and better-quality components. Despite advantages over traditional casting methods, thixoforming requires significant energy owing to rigorous thermal management and specialized equipment during reheating and forming.

The Shearing Cooling Roll (SCR) method, developed by Kiuchi & Sugiyama [21], presents a viable solution to existing challenges by merging intense shear deformation with rapid, accurate cooling in a single operation. Following the development of this process, Wang et al.[22] investigated the formation and evolution of microstructures during SCR processing and reported that the combined effect of rapid cooling and intense shear in the roll-shoe cavity promotes the transformation of dendritic structures into fine equiaxed grains. Although previous research has shown SCR's ability to convert dendritic α-Al structures into spherical morphologies, these studies have primarily focused on alloys such as Pb-Sn, A2017, A5056, ADC12, and various ferrous materials. The present study focuses on A356 alloy, a widely used cast aluminium alloy of considerable industrial significance, with no systematic studies reported under SCR processing conditions. The complex interplay among stress-strain response, microstructural evolution, and porosity formation in the semi-solid state remains unexplored. In particular, the effects of key processing parameters; such as speed of roll, roll-shoe gap, and grain refinement with intense shear. Modification of eutectic Si morphology and porosity suppression have also not been comprehensively established, highlighting the need to establish clear structure-property relationships under SCR processing conditions. In this study, a laboratory-scale SCR setup is developed for A356 Al alloy to examine the impacts of roll speed and roll-shoe gap on mechanical properties, microstructural refinement, and porosity of A356 aluminum alloy billets. Samples obtained from various regions within the SCR processing cavity are analyzed to study microstructural evolution, focusing on the transition

from dendritic to globular α-Al and the refinement of eutectic Si under varying processing parameters. Additionally, FEM simulations with a bilinear isotropic hardening model for semi-solid A356 are utilized to illustrate local stress-strain fields and correlate these with microstructural features observed experimentally. The integration of FEM analysis with detailed microstructural and mechanical assessments has facilitated the establishment of optimized processing parameters, resulting in the production of finer *α*-Al grains and diminished porosity.

2. Material and Methods

2.1 Design of experimental setup

The schematic of the SCR experimental setup is illustrated in Fig. 1, and its technical specifications are presented in **Table 1** for the semi-solid casting of aluminium A356 alloy. The setup comprises five key components:

i. Rotating roll and stationary shoe forming the cavity,
ii. Pouring channel guiding molten metal into the cavity
iii. Oil-cooling system for temperature control,
iv. Power drive with speed controller for roll rotation
v. Machine bed enabling cavity gap adjustment by moving the shoe.

The envisaged SCR setup dwells on the foundational design principles established by Kiuchi & Sugiyama [21], with critical modifications to enhance process control and analytical capabilities. The roll diameter is increased by 100mm in comparison to Kiuchi and Sugiyama to enhance the shear zone coverage and accommodate the cooling system to enable independent thermal management of both roll and shoe surfaces through dedicated oil circulation channels. A multi-axis sliding mechanism is introduced in the machine bed for precise adjustment of roll-shoe gap between 4 and 8 mm along with angular alignment across three planes. Integration of a flow guide, jacketed cavity and mold chamber, with argon purge system to maintain sealed operation under inert atmosphere forms novel part of this work as shown in image of the laboratory scale SCR setup Fig. 2**(a)**. Additionally, in-situ sampling ports are placed at multiple locations along the cavity length (top, middle, and bottom) enabling the extraction of semi-solid slurry at successive solidification stages; from the initial liquid-metal entry at the top region to the high-shear zone at the roll-shoe gap at the bottom. This spatially resolved sampling capability allows detailed study of microstructural evolution throughout the process. Correlating these location-specific microstructures with the corresponding temperature data recorded by thermocouples positioned at TC1, TC2, and TC3 as shown in Fig. 2**(b)**; provides detailed insight into the interaction between shear and cooling during processing.

The cast iron rotating roll (1), with a diameter of 500 mm and a width of 100 mm, is connected to a shaft (1A) that is driven through a pulley and belt system. The stationary shoe made of medium-carbon steel (2) and the roll together form a cavity where molten metal is sheared and agitated. Cooling channels

inside the roll and shoe allow continuous circulation of synthetic heat-treatment oil (flash point ≈ 400°C) with a flow rate of 5 LPM to maintain controlled thermal boundary conditions during processing. Rotary unions mounted at the shaft ends enable uninterrupted coolant flow during rotation. Maintaining a stable boundary temperature is essential for reliable cooling-rate estimation, as heat transfer at the roll–metal interface strongly influences solidification behavior, similar to the thermal boundary control reported in twin-roll casting processes as reported by Li *et al* [23]. The rotating roll provides shearing and friction, enabling rolling effect even at higher solid fractions. A jacket (3) seals the assembly and prevents splashing, and it includes three sample collectors (3A) for extracting melt during processing for microstructural analysis. The molten alloy is poured into the cavity through a flow guide (4A) that connects the furnace (4) to the upper surface of the shoe. Inside the cavity, the molten metal is cooled and sheared before exiting as semi-solid slurry. This slurry is drawn downward by the roll and ultimately exits through the gap between the roll and the shoe **(**Fig. 2b-2c**).** K-type thermocouples are positioned along the flow path inside the cavity at three locations (TC1, TC2, and TC3), as shown in Fig. 2b, and data are collected using SCADA software to map the temperature distribution across the slope. A stripper (5), at the cavity exit and linked to the mold chamber (6), directs flow and removes adhered material to the roll. The roll-shoe gap is adjustable with the shoe being movable. The machine bed (7) enables multi-directional and vertical movements to vary gap and slope. All components are securely connected, creating a continuous system that maintains a sealed environment suitable for an inert atmosphere. The power system (8) includes a 3.5 kW motor and 12:1 gearbox, driving the shaft through a belt-pulley arrangement with adjustable roll speed (0-120 RPM) using a variable frequency drive. The setup exhibits a compact and lightweight design as a result of its relatively low operational force and power requirements suitable for processing both ferrous and non-ferrous alloys.

2.2 Material Specification

A commercial A356 Al alloy was used in the present study. The chemical composition of A356 alloys is shown in **Table 2**.

2.3 Semi-Solid Casting Process Using SCR Setup

A 4 kg melt of A356 alloy was prepared at 650°C using a resistance-type non-ferrous melting furnace. After melting, the alloy was treated with modifying (0.1 wt.% Al-10Sr) and refining agents (0.15 wt.% Al-5Ti-1B).In order to remove dissolved gases, the melt was degassed with argon, after which it was furnace-cooled to 635°C before being poured into the melt-pouring crucible positioned above the flow guide attached to the cavity, as illustrated in Fig. 1.For the initial experiments and process development, two key parameters; roll speed and the gap between the shoe and roll were varied systematically with a constant pouring temperature of 635°C.To maintain a uniform wall temperature and remove moisture, hot oil at 200°C was circulated through the roll and shoe, and the mold was preheated to 350°C.The molten metal then entered the cavity through the flow guide at 635°C, which is slightly above the liquidus temperature (614°C) of the A356 alloy [15]. The slurry is continuously sheared as it cools and flows through the cavity. A series of experiments were conducted to investigate the influence of roll rotational speed and the effect of the roll-shoe gap. The roll speed was evaluated at three conditions: no rotation (0

RPM), low speed (40 RPM), and high speed (120 RPM). The roll-shoe gap was varied between 4 and 8 mm to assess the resulting trade-off. It is to be observed that the gap is not uniform along the periphery of the roll with the top end has a slightly wider gap than the bottom end to accommodate pouring and the gap measured at the bottom before pouring is used as the reference value for this study. To capture the temperature distribution across the SCR, sheathed K-type thermocouples (1 mm × 600 mm) connected to a GRAPHTEC GL240 (firmware 1.55; software 1.30)with sampling interval set at 100ms is introduced on three locations shown in Fig. 2**(b)**.Furthermore, cold-junction compensation (CJC) and channels were calibrated against a traceable reference and the uncertainties in measurement during the casting experiments were treated as direct measures of the accuracy of the instrumentation employed. The GL240 data logger and the K-type thermocouples (Aavad AKCS) constitute the primary sources of error, and their individual limits were combined according to standard uncertainty propagation. The uncertainty contributions associated with the temperature measurement arise from the thermocouple tolerance (as per IEC 60584 for Type K) and data logger measurement limits (CJC accuracy and quantization). The combined uncertainty associated with the temperature measurement is therefore obtained by the root-sum-square (RSS) method of the individual components as,

$$\delta_T = \sqrt{\delta_{daq}^2 + \delta_{th}^2}$$

1

…

Where δ_{th} represents the thermocouple tolerance term and δ_{daq}accounts for the GL240 contribution.

2.4. Heat Treatment

The microstructure and mechanical properties of the A356 alloy were enhanced through a T6 heat-treatment cycle. Cast blocks produced under different processing conditions were sectioned into rectangular specimens (150 × 70 × 20 mm) using a wire electrical discharge machine (WEDM, Taiwan; Model GX360L). The T6 heat treatment consisted of solutionizing the specimens in a muffle furnace at 540°C for 8 h to dissolve soluble phases and homogenize the matrix. The specimens were then quenched in water maintained at 70°C to retain a supersaturated solid solution. This was followed by artificial aging at 155°C for 6h to promote the controlled precipitation of fine Mg-Si strengthening phases (β"/β'), thereby achieving a balanced combination of strength and ductility in the cast A356 alloy. The interval between quenching and aging was minimized to avoid natural aging, and all specimens were cleaned prior to heat treatment to prevent surface contamination that could affect microstructural evolution.

2.5. Grain Size and Degree of Sphericity of Primary α-Al Particles

The size and sphericity of the primary α-Al phase were quantified by measuring two parameters: grain diameter and shape factor, using MATLAB (Image Processing Toolbox). For each processing condition,

eight non-overlapping fields of view (50 μm) were systematically selected at predetermined intervals across the top, middle, and bottom regions of the SCR cavity, with three independent samples used to ensure reproducibility. Micrographs were preprocessed through thresholding, noise filtering, and grain-boundary detection and the automated MATLAB measurements were validated against manual assessments across 20 fields, showing low deviation (± 2.1% in grain size and ± 3.8% in sphericity). In total, over 500 grains were analyzed per condition, yielding R^2 values of 0.92–0.96, confirming robust microstructural quantification. The resulting data, including average particle size and sphericity, were evaluated under different processing conditions. Grain diameter (G.D.) and shape factor (S.F.) were calculated using the following equations:

$$G.D. = 2\sqrt{\left(\mathrm{A}_{\alpha}/\pi\right)}$$

2

...

$$S.F. = \left(4\pi\, A_{\alpha}/P_{\alpha}^{2}\right)$$

3

...

Where, A_{α} and P_{α}represent the area and perimeter of the primary α-Al phase, respectively. Each globule is considered an individual grain. For optimal semi-solid processing, the shape factor should approach a value of 1, indicating a near-spherical morphology.

2.6. Microstructural and Fractographic Characterization

Standard metallographic procedures were used for sample preparation. Etching was carried out with Keller's reagent consisting of 2.5% HNO_3, 1.5% HCl, 1% HF, and 95% H_2O by volume. Phase assessment was performed using an optical microscope (Axio-Imager, Carl Zeiss, Germany). Microstructural analysis was conducted using a field-emission scanning electron microscope (FESEM, Σigma HD, Carl Zeiss, Germany) equipped with an EDX detector (X-Max, Oxford Instruments, UK). Fracture surfaces were examined using FESEM to evaluate fracture micro mechanisms. High-resolution characterization was performed using HRTEM (JEOL FE3200 FS, 300 kV). A 500 μm slice was extracted from the modified region by wire EDM, thinned to 90 μm, and a 3 mm disc was punched from the fusion zone. Final thinning was achieved through twin-jet electro polishing in a 95% ethanol + 5% perchloric acid solution until perforation occurred. Electron-transparent regions adjacent to the perforation were used for imaging. HRTEM and STEM bright-field and dark-field imaging were used to characterize the matrix features and nanoscale precipitates, while EDS was employed to obtain elemental information.

2.7. Density and Porosity Measurement

To assess the influence of microstructural coarsening and casting induced porosity on the stress-strain response of A356, the porosity was quantified as volumetric porosity by determining the bulk density of

the samples by the Archimedes method. Porosity is quantified as volumetric porosity by measuring the bulk density of samples using the Archimedes method. These measurements were then compared to the theoretical density of the alloy to calculate the micro-porosity content. The theoretical density (ρ) of the A356 aluminium alloy was calculated based on its chemical composition and the densities of its constituent elements. The calculation uses the rule of mixtures as follows:

$$\rho = \left(\frac{1}{\sum_i \left[\frac{wi}{\rho\, i}\right]}\right) \ldots (4)$$

where, w_i is the weight fraction of the i^{th} element and ρ_i is the density of the i^{th} element respectively. The theoretical density of the A356 alloy is calculated as 2.670 g/cm³ using the weighted average density based on its chemical composition. Porosity of the samples was determined by comparing the experimentally measured bulk density to this theoretical density, using the following formula:

$$\Phi = \left(\frac{\rho_{ex-\rho\ th}}{\rho_{ex}}\right) \times 100 \ldots (5)$$

where, ρ_{ex} = experimental density calculated by Archimedes method and ρ_{th} = theoretical density.

2.8. Finite Element Analysis

During casting, the alloy was subjected to continuous shear, promoting a fine, non-dendritic microstructure that enhance thixotropic flow behavior in the semi-solid state. In the temperature range of 560–580°C, A356 alloy exhibits a high solid fraction based on the experiments conducted by Sheykh-jaberi *et al.* [24] in Fig. 3, indicating that the solid phase remains dominant within the semi-solid slurry. This high solid content significantly affects the material's flow behavior, as the interconnected solid phase continues to bear mechanical loads and influences stress distribution within the semi-solid mass confined inside the cavity.

Consequently, the rheological behavior of the semi-solid alloy cannot be accurately represented using models developed for purely solid or purely liquid materials, since small temperature variations within this narrow semi-solid range produce large changes in the solid fraction and mechanical response. The stress-strain behavior under semi-solid conditions considered in the simulation studies was obtained based on the experimental data reported by Yao *et al.* [25] and a bilinear elastic-plastic approximation, commonly used in metal forming simulations [26], was implemented in ANSYS to describe the mechanical response of semi-solid A356.

This model efficiently captures the visco-plastic response of semi-solid alloys dominated by solid phase [24, 27]. The cavity domain was discretized using 3D, 20-node, higher-order element with quadratic interpolation, suitable for simulating large strains, nonlinear deformation, and stress localization [28]. A refined mesh was employed in regions of expected stress concentration as seen in Fig. 4 and additionally, a grid independence study was conducted to assess the adequacy and influence of the element count on the simulation results.

2.9. Tensile Testing and Hardness Measurement

Flat tensile specimens with a gauge length of 30 mm and a cross-section of 6 mm × 6 mm were machined from the alloy according to ASTM E-8M standards. Tensile tests were performed at room temperature using a universal testing machine (UTM Model: Median-100, BISS, India) at a crosshead speed of 0.5 mm/min (strain rate of 2.7×10^{-4} s^{-1}). Reported tensile strength values represent the average of at least three specimens. Vickers hardness (HV5) measurements were conducted using a Vickers hardness tester under a 5 kgf load, with hardness values averaged from at least ten symmetrical indentations.

3. Results and Discussion:

3.1 Microstructural Evolution

The transition from dendritic to globular α-Al during semi-solid processing is well established and results from the combined action of shear deformation, rapid cooling, and solute diffusion during partial melting [5]. In semi-solid metal processing, grain refinement is promoted by rapid heat extraction, increased nucleation, and shear-induced fragmentation, which favor the formation of fine equiaxed globular microstructures in the semi-solid slurry [29]. Fragmentation of dendrite arms during semi-solid processing promotes the formation of refined equiaxed α-Al grains, as forced convection and remelting during shearing suppress dendritic growth and produce globular microstructures in A356 alloy. Such grain refinement improves the uniformity of the semi-solid slurry and favors the formation of stable non-dendritic structures. Similar behavior has been reported in rheocast and semisolid-processed A356 alloys, where reduced grain size and increased sphericity of the primary α-Al phase resulting in improved mechanical properties [30, 31]. Higher intensity forced melt flow, generated by the rotating roll in the Shearing Cooling Roll (SCR) process employed in this study, refines the microstructure substantially, producing fine α-Al cells distributed in a compact eutectic network (Fig. 5). T6 heat treatment further spheroidizes eutectic silicon, yielding a stable, homogenized microstructure. The eutectic Si, which appears as coarse flakes in gravity-cast A356, transforms into fine lamellar and spheroidized particles as shown in (Fig. 5). To further explain these mechanisms, a series of SCR experiments are carried out to evaluate microstructure evolution under uniform cooling and high shear. Samples taken from the top, middle, and exit of the cavity enable correlation of positional variations in shear rate and cooling with the resulting *α*-Al cell size and eutectic Si morphology. As shown in Fig. 6, the microstructure transitions from dendritic features at the top to refined, near-spheroidal *α*-Al grains at the exit, corresponding to increased shear intensity in the narrowing gap. The semi-solid slurry exiting the cavity exhibits a coherent, strip-like morphology (Fig. 2c**)** suggesting that even high solid-fraction slurries can sustain continuous, shear-driven flow under roll rotation, exhibiting viscous-plastic flow behavior consistent with observations reported by Kiuchi and Sugiyama [21]. Optical micrographs (Fig. 7) show that rapid cooling from both walls of the cavity preserves these transient microstructural states, highlighting the interplay between shearing and cooling. Higher cooling rates at the wall surfaces refine the eutectic lamellae and

promote extensive surface nucleation. In addition; shear forces fragment dendrites and redistribute solute, contributing to the overall microstructure evolution [32]. As the molten metal flows through the cavity, superheat dissipation initiates nucleation at the roll and shoe surfaces, generating a high density of solid grains through rapid heat extraction and melt convection. These nuclei subsequently detach and disperse into the melt, generating rosette-shaped and near-spherical particles as shown in Figs. 6–7. A similar microstructural evolution during SCR processing was reported by Wang *et al.* [22], stating that dendrites first nucleate on the roll and shoe surfaces and are then fragmented by intense shear generated by the rotating roll, producing fine equiaxed grains in the semi-solid slurry. In the regions of low shear and slower cooling, such as the cavity top, *α*-Al grains remain as partially fragmented rosettes with entrapped liquid. As shear and cooling rate increases within the cavity, dendrite fragmentation, remelting, and particle separation promote spheroidization through coalescence and coarsening mechanisms. The microstructures observed across the cavity comprising fragmented dendrites, rosettes, and spheroidal *α*-Al grains confirm the simultaneous action of two dominant mechanisms: shear-induced crystal separation and surface-driven crystal multiplication via copious nucleation [32]. The degree of sphericity increases toward the cavity exit, where higher shear and melt flow enhance dendrite arm fragmentation by promoting remelting and detachment at the dendrite roots. The shear intensity and cooling rate necessary to achieve the desired outcome are governed by the roll-shoe gap and roll speed, which are the primary parameters.

Excessive shear can entrap gases due to turbulence, intensify thermal non-uniformity near the shear zone, and accelerate equipment wear. Insufficient shear, on the other hand preserves stress-concentrating dendritic microstructures, with pronounced micro segregation. As shown in Fig. 8, reducing the gap from 8 mm to 4 mm at a constant roll speed of 120 RPM enhances heat extraction at the contact surfaces. The higher cooling rate increases the rate of nucleation, leading to the formation of finer grains. The corresponding reduction in grain size **(**Fig. 8**)** further confirms the increased nucleation and accelerated fragmentation induced by higher shear-cooling conditions. In previously reported semi-solid processing routes [11, 12, 20], the primary*α*-Al grain size is generally in the range of 30–80 μm, whereas the SCR process produces substantially finer grains of about 20 μm in comparable conditions, demonstrating superior grain-refinement efficiency and lower energy demand. This refinement is governed by the roll-shoe gap and roll speed, which control the shear intensity and cooling rate within the cavity. Smaller gaps, such as 4 mm, restrict slurry flow due to premature solidification, resulting in poor mould filling and increased porosity. In contrast, wider gaps (8 mm) reduce shear intensity and produce coarser α-Al cells with entrapped eutectic pools. An optimal condition is obtained at a 6 mm gap, where sufficient shear strain is maintained for effective dendrite fragmentation without loss of flowability. Roll speed further affects the microstructure evolution; increasing the speed from 40 to 120 RPM at a 6 mm gap intensifies shear. The A356 alloy processed by SCR process exhibits a phase constitution comprising *α*-Al, Si, and Mg_2Si, as confirmed by the X-ray diffraction patterns shown in Fig. 9. In BF-TEM images, these dispersoids appear as dark, high-contrast features owing to their strong diffraction and the strain fields that develop around these hard precipitates. Their uniform distribution significantly enhances dislocation particle interactions as evidenced by dislocation bowing shown by arrows in Fig. 9,

suggesting Orowan looping and consequent hindrance to dislocation motion. EDS analysis confirmed the presence of Al, Si, and Mg, although the exact stoichiometry could not be determined because of the extremely small size of these precipitates. Based on their morphology, size, and composition, these nanoscale precipitates can be attributed to the β" phase, which is well established as the primary strengthening phase in peak-aged A356 alloy. Previous studies on peak-aged A356 alloys have shown that the formation of fine needle-like β" precipitates play a dominant role in precipitation hardening through coherency strain strengthening and interaction with moving dislocations [33, 34]. The β" phase, characterized by its needle-like morphology and nanoscale dimensions, plays a critical role in the precipitation hardening of A356 Al alloy, leading to enhanced mechanical properties [33]. The slight elongation of several diffraction spots indicates localized lattice distortion caused by dislocation fields, aligning with the deformation introduced during SCR and the subsequent interaction of dislocations with coherent nano-scale precipitates. In the present work, peak hardening appears to be governed by the combined effect of coherency strengthening from β" precipitates and dislocation bowing around SCR-refined Si dispersoids, which act as strong obstacles to dislocation motion. The BF-TEM image **(**Fig. 9**)** indicates a uniform dispersion and high density of nano-scale precipitates, which enhances dislocation-particle interaction and contributes to the observed strengthening.

3.2 Porosity

The deleterious effects of porosity in gravity-cast Al alloys are well documented, with volumetric pores initiating premature fracture and causing severe losses in ductility and tensile strength [9]. Porosity in aluminum alloys is a complex phenomenon driven by the interaction of dissolved hydrogen and metal shrinkage during solidification. Porosity forms when hydrogen, exceeding its solubility, creates bubbles that are then further influenced and expanded by the physical shrinkage of the metal during solidification, with various pressures dictating the ultimate size and formation of these pores [35]. SCR processing suppresses pore formation through two synergistic mechanisms: shear-induced fragmentation of dendritic networks that reduces inter-dendritic liquid entrapment, and roll-applied pressure that increases metallostatic pressure during solidification to counteract shrinkage- and gas-driven pore nucleation. A comparison of the SCR-processed samples with the as-cast specimen shows that shrinkage porosity is predominant in the as-cast sample as shown in Fig. 10**(a).** The samples processed without rotation contain a mixture of shrinkage and gas pores, whereas the samples processed at 40 and 120 RPM primarily exhibit micro-porosity Fig. 10**(a-e).** The quantitative analysis of bulk porosity and the corresponding variation in mechanical properties as porosity decreases is depicted by Fig. 11. These findings align with existing studies on the pronounced effect of micro-porosity on the tensile behavior of aluminium alloys [9, 36, 37]. In particular, samples processed at 120 RPM with a 6 mm roll gap (Fig. 10e) exhibit an almost complete elimination of shrinkage porosity and an approximately 75% reduction in bulk porosity compared with conventional casting. This can be attributed to semi-solid slurry flow and solidification under elevated pressure, producing a denser and more uniform microstructure with fewer internal defects. Similar densification under applied pressure has been reported in semi-solid forming processes, indicating that pressure-assisted solidification plays an

important role in suppressing porosity [37]. Increasing roll speed from 0 to 120 RPM at the 6 mm gap decreases volumetric porosity and subsequently increasing UTS values from 175 MPa to 240 MPa and elongation from 8.7% to 16.5%. Dual-wall cooling at narrower roll gaps like 4 mm produces high solid fractions and limits hydrogen diffusion, thereby suppressing pore growth. At high solid fractions, the permeability of the semi-solid network decreases, restricting liquid feeding during solidification and promoting pore formation when shrinkage cannot be compensated [38]. The fine inter-granular channels and reduced liquid reservoir lower permeability and restricts the liquid flow needed to accommodate interstitial expansion, leading to the entrapment of dissolved gases like hydrogen. However, the associated high cooling rates can promote localized solute segregation and lead to the formation of irregular, surface-connected micro-pores (Fig. 10f). These surface-connected defects impair elongation more severely than subsurface pores, resulting in the more pronounced ductility loss observed in high-porosity samples. The intensified heat extraction enhances solute segregation, and the irregular, surface-connected micro-pores shown in Fig. 10f further corroborate a segregation-controlled mechanism of porosity formation. These combined thermal and flow constraints collectively increase porosity in the 4 mm gap samples. The refined eutectic Si and globular α-Al matrix generated during SCR contribute additional strengthening and restrict crack propagation, complementing porosity reduction to improve mechanical performance. As shown in Fig. 11, the lowest porosity condition at 120 RPM and a 6 mm gap yields the highest YS, UTS, and elongation.

3.3 Mechanical Properties

The mechanical properties of SCR-processed A356 are governed by the combined effects of microstructural refinement, porosity suppression, and precipitation hardening developed during SCR processing followed by T6 heat treatment. Increased shear intensity and effective cooling during SCR refine the α-Al grains and modify the eutectic Si morphology, while the pressure exerted by the rotating roll during solidification suppresses shrinkage porosity and improves the structural integrity of the alloy. In addition, the formation of fine β" precipitates during aging contributes to precipitation strengthening, resulting in a combined strengthening effect that controls both hardness and tensile behavior. The evolution of hardness in SCR-processed and heat treated A356 Figs. 12**(a-b)**, reflects the combined influence of roll speed, roll-shoe gap, and the resulting microstructural refinement. Increasing roll speed from 0 to 120 RPM at a 6 mm gap increases hardness from 76 HV to 105 HV, while decreasing the gap to 4 mm at 120 RPM further increases hardness to 110HV. At the 4 mm gap, the process imposes the highest shear intensity and fastest cooling due to maximum wall contact and reduced solid fraction as well as slurry volume, producing the most refined microstructure. The enhanced hardness originates from two coupled mechanisms. First, higher shear intensity and cooling rate at narrower gaps promote fragmentation of primary α-Al dendrites and the formation of fine rosette-like and spheroidal particles, as reported for semi-solid alloys under forced convection [2]. This microstructural refinement increases resistance to dislocation motion, consistent with Hall-Petch strengthening, in which the flow stress increases with decreasing grain size due to the resistance to dislocation motion provided by grain boundaries [39, 40]. Second, compressive roll pressure during SCR processing increases dislocation

density and suppresses pore nucleation, thereby increasing the effective load-bearing area. HRTEM analysis of the heat-treated samples shows coherent precipitates that generate coherency strain and promote orowan looping, accounting for the additional increase in hardness. The shift from rosette-dominated morphologies at 40 RPM-6 mm and 120 RPM-8 mm to fully globular structures at 120 RPM-6 mm and 120 RPM-4 mm (Fig. 7) follows the same trend. T6 heat treatment further enhances the hardness response by modifying the eutectic Si morphology and promoting precipitation strengthening. Solution treatment fragments and spheroidizes eutectic Si platelets, as reported for heat-treated A356 alloys [41], while subsequent aging promotes the formation of fine strengthening precipitates in the α-Al matrix. Literature consistently shows that hardness in Al-7Si-Mg alloys increases when processing routes and heat treatment refine eutectic Si, restrict coarsening and form supersaturated solid solutions of Si and Mg in the Al phase, followed by the precipitation of Mg_2Si and other phases during aging [42, 43]. Tahamtan et al.[7] reported that the gravity-cast A356 alloy exhibited a hardness of 49.6 ± 0.6 HV, while rheocasting resulted in a marginal improvement to 50.1 ± 0.3 HV. Further processing through thixoforming resulted in a significant increase in hardness, reaching 73.7 ± 0.3 HV at 590°C and 61.3 ± 1.2 HV at 600°C. After T6 heat treatment, hardness increased for all processing routes, with gravity-cast, rheocast and thixoformed samples attaining 88.4 ± 0.4 HV and 88.9 ± 0.22 HV, 115 ± 0.21 HV at 590°C and 103.5 ± 0.3 HV at 600°C respectively. The enhanced hardness in thixoformed samples is attributed to reduced porosity, increased dislocation density, and improved microstructural uniformity. Birol [19] demonstrated that cooling slope-processed and thixoformed A390 alloy achieves hardness as high as 144 HB in T6 condition, which is significantly higher than conventional die-cast counterparts due to reduced porosity and uniform distribution of primary silicon particles. Similarly, A356 alloy produced via the gas-induced semi-solid (GISS) process attains a peak hardness of 96.4 HRE after aging at 165°C for 18 h, attributed to precipitation hardening by Mg–Si phases. Their study further indicates that hardness initially increases with aging time due to precipitation strengthening and subsequently decreases upon over-aging [33]. Gebril et al. [44] processed A356 alloy using the cooling-slope rheocasting technique to produce a globular semi-solid microstructure, followed by T6 heat treatment and subsequent severe plastic deformation methods such as equal-channel angular pressing (ECAP) and high-pressure torsion (HPT). The hardness of the alloy increased from 61 HV in the as-cast condition to 83 HV after cooling-slope processing due to grain refinement and transformation of dendritic α-Al into a globular structure. Further improvement after T6 heat treatment was attributed to spheroidization of eutectic Si and precipitation of Mg_2Si. Upon application of severe plastic deformation, the hardness increased significantly, reaching 134 HV after six ECAP passes and 211 HV after five HPT turns. In comparison to other semi solid processes, SCR-processed A356 alloy achieves 105 HV at 120 RPM-6 mm and 110 HV at 120 RPM-4 mm, representing significant improvement as compared to gravity cast and other rheocasting processes. Although these values are lower than those achieved by severe plastic deformation techniques SCR-processed material could plausibly attain comparable hardness if subjected to similar post-deformation methods, which lie outside the scope of the present study.

The tensile properties measured for SCR-processed A356 reflect the same underlying microstructural refinements that govern the hardness response, with strength and ductility determined by the combined

effects of α-Al globularization, eutectic-Si fragmentation, porosity suppression, and the subsequent precipitation. TEM analysis (Fig. 9) confirms that T6 ageing coherently dispersed precipitates and impose substantial resistance to dislocation movement through coherency-strain strengthening and orowan looping. Their presence directly contributes to the increases in yield strength and ultimate tensile strength observed after ageing, whereas the reduction in elongation reflects the restricted plastic deformation that develops once dislocation-precipitate interactions begin to control the flow behavior. Yang *et al.* [45] observed that reduced elongation in A356 aluminum alloy under tension is primarily due to premature fracture caused by initial cast pores and the initiation and propagation of micro cracks at the interface between hard eutectic silicon particles and the softer aluminum matrix. Microstructural control via heat treatment is essential for enhancing ductility, since the morphology of eutectic silicon particles significantly affects crack initiation and fracture behavior [45, 46].

The samples processed by SCR demonstrate substantial increment in yield strength, ultimate tensile strength and reasonable ductility as shown in **Table 3**, with performance consistently exceeding that of conventional gravity-cast, cooling-slope, and other semi solid processing routes as discussed earlier. T6 heat treatment further intensifies this strengthening through the formation of precipitates; however, the associated decrease in ductility reflects the classical strength-ductility trade-off induced by precipitation hardening and the increasing constraint that hard eutectic Si/Mg_2Si phases impose on matrix plasticity. For 0 RPM, 6 mm gap, the SCR process attains yield strength of 220 MPa and UTS of 275 MPa with 6.2% elongation post T6. Although superior to gravity-cast counterparts, these values remain below tensile strength of 293 MPa and 15% elongation, reported for cooling-slope processing by Haga & Kapranos [47], attributable to residual porosity and incomplete eutectic refinement. In 120 RPM, 4 mm gap, the hardness increases from intensified shear and rapid cooling that refine α-Al grains and eutectic Si, whereas the reduced elongation results from restricted feeding and segregation driven surface connected micro porosity. This condition therefore reflects a trade-off in which grain refinement enhances hardness, but pore formation and localized segregation limit ductility. At moderate shear (40 RPM, 6 mm gap), T6 ageing produces significant strength increments, 131 MPa to 225 MPa in yield strength and 182 MPa to 282 MPa in ultimate tensile strength with decrement in elongation from 7.5% to 5.72% due to crack initiation at coarse Si platelets. The optimized SCR condition (120 RPM, 6 mm gap) provides the highest tensile properties, with T6-treated samples reaching yield strength of 276 MPa and UTS of 330 MPa with elongation of 11.6% showing notable improvement in mechanical properties over widely reported semi-solid processing methods. These values show a higher ultimate tensile strength of 330 MPa compared to 260.74 MPa reported for rheological squeeze casting with T6 treatment by Xiong *et al.* [10], along with a slightly higher elongation of 11.6% compared to 10.03%, indicating more effective microstructural refinement and defect reduction in the SCR process. Compared to the cooling-slope rheocasting process reported by Haga & Kapranos [18], the SCR condition exhibits higher tensile strength and yield strength than the reported values of 310 MPa UTS and 241 MPa YS, respectively. However, the elongation of 11.6% is lower than the 18% achieved by cooling slope, indicating a trade-off toward strength due to finer microstructure and reduced porosity. Tahamtan *et al.* [7], using rheocasting followed by T6 heat treatment, reported tensile properties of approximately 212 MPa UTS and 4.7%

elongation, which are significantly lower than those obtained under the present SCR condition. Although thixoformed samples in their study exhibited higher peak values of ~ 378 MPa UTS and 24.5% elongation, the comparison with SCR is more appropriately made with the rheocast condition. Tensile results of present study also exceed those of thixoformed A356 reported by Kumar *et al.* [46] by approximately 12% in yield strength and 6% in UTS, reflecting the combined effects of globular *α*-Al grains, refined eutectic Si, and lowest porosity levels. Compared to the rheocast condition reported by Jin [11], where a tensile strength of 205 MPa and elongation of 9.8% were obtained, the SCR condition provides significantly higher strength with comparable ductility. In addition, it has been reported that thixoforming reduced the α-Al grain size and improved sphericity, increasing strength to ~ 265 MPa while reducing elongation to 6.9%, whereas the SCR samples achieve higher strength through a single-step shear-assisted casting process, eliminating the need for additional stages such as reheating, upsetting, and thixoforming, while still ensuring effective grain refinement, enhanced α-Al globularity, and reduced porosity. Overall, the superior performance of the SCR samples is attributed to the combined effects of globular α-Al grains, refined eutectic Si morphology, and minimal porosity, leading to an optimal balance of strength and ductility. The results collectively show that SCR allows for precise control of shear intensity and thermal gradients, enabling the tailoring of the strength-ductility profile, substantial porosity reduction, significant grain refinement, and the production of high-integrity microstructures suitable for demanding automotive applications.

3.4 FEM Analysis

The FEM simulations provide critical insights into the mechanisms governing microstructural refinement and mechanical enhancement in SCR-processed A356. The temperature distribution across the SCR cavity, measured at three locations (TC1, TC2, and TC3) as shown in Fig. 2**(b)**, indicates that the exit temperature of the semi-solid slurry is approximately 570°C, as confirmed by thermocouple data **(**Fig. 13**)**. The stress-strain data of A356 slurry at 570°C [24] as seen in Fig. 3 is considered for the simulation at constant temperature, since the temperature drop is within 2% across the entire travel length. This approach is consistent with previous semi-solid deformation studies based on casting and forging, where material behavior is evaluated at constant temperature within the semi-solid range [24, 25]. As shown in Fig. 14**(a-b)**, peak shear stress 0.33 MPa for 120 RPM, 6mm gap process at 0.82 s occurs at the billet-roll interface due to intense friction and high solid fraction impeding the flow through cavity. At 570°C, the alloy contains a high solid fraction 0.8, and the interconnected solid network carries most of the applied load, leading to higher stress levels under deformation. Similar behavior has been reported in semi-solid deformation studies, where increase in solid fraction enhances the load-bearing capacity of the material [24].

This localized stress concentration near the interface is likely to contribute to the breakdown of dendritic structures that is associated with the formation of more equiaxed or globular grains, commonly observed in semi-solid processing. This behavior is consistent with dendrite fragmentation and spheroidal grain formation near the cavity exit **(**Figs. 6–7**)**, where fragmentation and re-melting mechanisms are dominant [32]. The FEM-predicted strain distribution **(**Fig. 15a**)** further elucidates the

microstructural evolution, showing a peak total strain of 0.362 at the billet-roll interface for same processing condition. The corresponding shear stress distribution (Fig. 15b) also highlights this region as the primary deformation zone, consistent with dendritic arm fragmentation and microstructural refinement. This localized strain may facilitate dynamic recrystallization, aiding the transformation of fragments into spheroidal grains through mechanisms such as localized re-melting and shear-induced coalescence [27]. The visco-plastic nature of the semi-solid matrix, as indicated by the non-uniform deformation distribution (Fig. 16), is consistent with the flow behavior commonly reported in semi-solid deformation studies [25]. Furthermore, the variation in stress across different regions is a key factor in the development of the microstructural gradient observed in SCR processing (Fig. 6). Fine globular grains are observed in the narrower regions near the cavity exit, whereas larger rosette structures are retained in the middle portion of cavity.

3.5 Fractographic analysis:

The fracture behavior of SCR-processed A356 alloys is strongly influenced by microstructural features, particularly the morphology of eutectic Si particles and the continuity of the α-Al matrix. The interaction between these phases governs crack initiation and propagation during tensile loading. Gu et al.[48] reported that A356 alloys exhibit a mixed fracture mode consisting of dimples, tear ridges, and quasi-cleavage features, reflecting the combined modes of fracture. In addition, Yang et al. [9] showed that microcracks preferentially initiate at the edges of casting pores due to localized stress concentration, while fracture and debonding of eutectic Si particles also act as primary crack initiation sites. Microcracks during tensile deformation often initiate at the interface between eutectic Si particles and the aluminum matrix, subsequently propagating through the α-Al dendrites and leading to final fracture [45]. Refinement and spheroidization of eutectic Si particles reduce stress concentration and improve ductility. During deformation, void nucleation at Si particles contributes to dimpled fracture morphology (Fig. 17a), whereas coarse and acicular Si promotes cleavage-like features and a more brittle response [44]. In the present study (Fig. 17a-17b), similar fracture features are observed. Tensile failure in rheocast samples occurs through a combination of dimple rupture and flat fracture facets, with crack initiation often at the interface between eutectic Si particles and the aluminum matrix. A clear transition in fracture mode is observed with increasing shear rate at a 6 mm gap as depicted in Fig. 17a. At lower shear (40 RPM), fracture surfaces exhibit cleavage facets, porosity, and microcracks, indicating a predominantly brittle response. With increase in shear rate (120 RPM, 6mm) fracture morphology transitions to ductile mode characterised by fine, uniformly distributed dimples via micro void coalescence. This improvement is attributed to the refinement of coarse, acicular Si into more spheroidal particles under higher shear, resulting in reduced stress localization and delayed crack initiation. For varying gap at 120 RPM (Fig. 17b), the 6 mm sample exhibits the most uniform dimple morphology and minimal defect features, whereas the 4 mm and 8 mm samples display larger voids and localized stress concentration features. These differences suggest that both insufficient and excessive gap can lead to microstructural inhomogeneity and reduced fracture resistance. T6 heat treatment further enhances fracture behavior by modifying the eutectic Si morphology through fragmentation and spheroidization,

along with precipitation strengthening of the matrix. Overall, processing at 120 RPM with a 6 mm gap, followed by heat treatment, produces a refined and globular microstructure that enhances both strength and elongation.

4. Conclusion

1. SCR transforms dendritic A356 into spheroidal *α*-Al grains and refines eutectic Si through high shear. This microstructural refinement, coupled with a notable reduction in porosity, yields a fine grained, defect minimized matrix that markedly enhances the mechanical strength and reliability of the alloy for high performance engineering applications.
2. SCR-processed A356 at a roll speed of 120 RPM with a 6 mm gap attains an ultimate tensile strength (UTS) of 330 MPa (post-T6), a significant improvement over conventional casting and rheocasting routes, while achieving comparable performance to thixoforming processes. The corresponding hardness value of 105 HV also reflects 8% improvement compared to the cooling slope method. These enhancements are attributed to grain refinement and increased dislocation density, collectively contributing to an optimized strength-ductility balance.
3. FEM simulations show that at 120 RPM and a 6 mm gap, a peak shear stress of ~ 0.33 MPa promotes dendrite fragmentation and spheroidization, producing finer globular α-Al grains and improved mechanical properties. In contrast, lower shear at 40 RPM leads to incomplete fragmentation, retaining rosette-like microstructures and reducing UTS.
4. The globular microstructure produced by the SCR process promotes a predominantly dimpled fracture mode, reducing stress concentration and minimizing the fracture of eutectic Si platelets. Subsequent T6 heat treatment further enhances fracture resistance through Si spheroidization, and precipitation strengthening improving both ductility and strength.

Declarations

Declaration of generative AI and AI-assisted technologies in the writing process: During the preparation of this work the author used Generative-AI tools Open AI ChatGPT for paraphrasing. After using this tool/service, the authors reviewed and edited the content as needed and take full responsibility for the content of the published article.

Conflict of interest:

The authors declare no competing interests.

Ethics approval:

Not applicable.

Consent to participate:

Not applicable.

Consent for publication:

Not applicable.

Funding:

The funding of the work is by CSIR-Central Mechanical Engineering Research Institute, India.

Author Contributions:

Ruchika Dhyani: Conceptualization, Methodology, Writing - original draft, Writing- review & editing, Design and Development of Experimental Setup, Planned and Performed the Experiments, Investigation, Formal analysis, Data curation. **Prashant Tadge**: Design and Development of Setup, Drawing of Various Parts of the Setup. **Balaji Chandrakanth**: Data Analysis for FEM. **Harsh Bhakta**: FEM Analysis. **Adwaita Maity**: Planned and Performed the Experiments. **Himadri Roy**: Project Administration, Writing - review & editing, Supervision. **Dipankar Chatterjee**: Writing - review & editing, Supervision. **Sudip Samanta**: Supervision, Project Administration, Funding acquisition & Resources.

Acknowledgements:

The authors would like to thank the Director, CSIR-CMERI Durgapur, AcSIR coordinator, Dr. Pranab Samanta, and members of Advanced Casting Research Group, CSIR-CMERI, Durgapur for their constant support and motivation throughout the work.

Data availability:

The authors confirm that the data supporting the findings of this study are available within the article

Materials availability:

The authors confirm that the data supporting the findings of this study are available within the article

Code availability:

Not applicable.

References

1. Flemings MC, Riek RG, Young KP (1976) Rheocasting Mater Sci Eng 25:103–117. https://doi.org/10.1016/0025-5416(76)90057-4
2. Flemings MC (1991) Behavior of metal alloys in the semisolid state. Metall Trans B 22:269–293. https://doi.org/10.1007/BF02651227
3. CHEN CY, SEKHAR DGB JA and RM (1979) Thixoforging of Aluminum Alloys. Mater Sci Eng 40:265–272. https://doi.org/10.1016/0025-5416(79)90198-8
4. Spencer DB, Mehrabian R, Flemings MC (1972) Rheological behavior of Sn-15 pct Pb in the crystallization range. Metall Trans 3:1925–1932. https://doi.org/10.1007/BF02642580
5. Fan Z (2002) Semisolid metal processing. Int Mater Rev 47:49–85. https://doi.org/10.1179/095066001225001076
6. Mohammed MN, Omar MZ, Salleh MS et al (2013) Semisolid metal processing techniques for nondendritic feedstock production. Sci World J 2013. https://doi.org/10.1155/2013/752175
7. Tahamtan S, Boostani AF, Nazemi H (2009) Mechanical properties and fracture behavior of thixoformed, rheocast and gravity-cast A356 alloy. J Alloys Compd 468:107–114. https://doi.org/10.1016/j.jallcom.2007.12.079
8. Nafisi S, Ghomashchi R (2005) Semi-solid metal processing routes: An overview. Can Metall Q 44:289–304. https://doi.org/10.1179/cmq.2005.44.3.289
9. Yang BC, Chen SF, Song HW et al (2022) Effects of microstructure coarsening and casting pores on the tensile and fatigue properties of cast A356-T6 aluminum alloy: A comparative investigation. Mater Sci Eng A 857:144106. https://doi.org/10.1016/j.msea.2022.144106
10. Xiong W, Wei K, Wang K et al (2025) A novel semi-solid rheo-squeeze strategy for optimizing the microstructure and mechanical properties of A356 aluminum alloy. J Sci Adv Mater Devices 10. https://doi.org/10.1016/j.jsamd.2025.101050
11. Jin CK (2022) Microstructures and Mechanical Properties of A356 Alloy and A6061 Alloy through Rheo, Upsetting, Thixo, Forming Process, and T6 Heat Treatment. Metals (Basel) 12:. https://doi.org/10.3390/met12122051
12. Deepak Kumar S, Mandal A, Chakraborty M (2014) Cooling Slope Casting Process of Semi-solid Aluminum Alloys: A Review. Int J Eng Res Technol 3:269–283
13. Doherty RD, Lee H (1984) Microstructure of Stir-cast Metals. Mater Sci Eng 65:181–189. https://doi.org/10.1016/0025-5416(84)90211-8
14. Kang CG, Lee SM (2008) Development of a new rheology forming process with a vertical-type sleeve with electromagnetic stirring. Int J Adv Manuf Technol 39:462–473. https://doi.org/10.1007/s00170-007-1242-2
15. Jian X, Xu H, Meek TT, Han Q (2005) Effect of power ultrasound on solidification of aluminum A356 alloy. Mater Lett 59:190–193. https://doi.org/10.1016/j.matlet.2004.09.027

16. Ji S (2003) The fragmentation of primary dendrites during shearing in semisolid processing. J Mater Sci 38:1559–1564. https://doi.org/10.1023/A:1022945219926
17. Tzimas E, Zavaliangos A (2000) Evolution of near-equiaxed microstructure in the semisolid state. Mater Sci Eng A 289:228–240. https://doi.org/10.1016/S0921-5093(00)00908-4
18. Haga T, Kapranos P (2002) Simple rheocasting processes. J Mater Process Technol 130–131:594–598. https://doi.org/10.1016/S0924-0136(02)00819-1
19. Birol Y (2008) Cooling slope casting and thixoforming of hypereutectic A390 alloy. J Mater Process Technol 207:200–203. https://doi.org/10.1016/j.jmatprotec.2007.12.071
20. Das P, Samanta SK, Ray T, Venkatpathi BRK (2012) Mechanical properties and tensile fracture mechanism of rheocast A356 Al alloy using cooling slope. Adv Mater Res 585:354–358. https://doi.org/10.4028/www.scientific.net/AMR.585.354
21. Kiuchi M, Sugiyama S (1995) A New Process to Manufacture Semi-solid Alloys. ISIJ Int 35:790–797. https://doi.org/10.2355/isijinternational.35.790
22. Wang S, Cao F, Guan R, Wen J (2006) Formation and evolution of non-dendritic microstructures of semi-solid alloys prepared by shearing/cooling roll process. J Mater Sci Technol 22:195–199
23. Li JT, Xu GM, Yu HL et al (2015) Optimization of process parameters in twin-roll strip casting of an AZ61 alloy by experiments and simulations. Int J Adv Manuf Technol 76:1769–1781. https://doi.org/10.1007/s00170-014-6312-7
24. Sheykh-jaberi F, Cockcroft SL, Maijer DM, Phillion AB (2019) Comparison of the semi-solid constitutive behaviour of A356 and B206 aluminum foundry alloys. J Mater Process Technol 266:37–45. https://doi.org/10.1016/j.jmatprotec.2018.10.029
25. Yao Z, Mei D, Tang P, Chen Z (2014) On the size effects in micro/meso semisolid extrusion-forging of A356 aluminum alloy. Int J Adv Manuf Technol 73:1243–1252. https://doi.org/10.1007/s00170-014-5912-6
26. Wagoner RH, Chenot JL (2001) Metal Forming Analysis. Cambridge University Press
27. Boluri Gashti AH, Abedi HR, Salehi MT (2023) Microstructure evolution and constitutive modeling of as-cast A356 aluminum alloy in semi-solid deformation regime. J Mater Res Technol 24:7720–7731. https://doi.org/10.1016/j.jmrt.2023.05.025
28. Inc. A (2023) ANSYS Mechanical APDL Theory Reference
29. Tajudin MFM, Ahmad AH, Alias J et al (2023) Grain refinement in semi-solid metal processing: current status and recent development. Int J Adv Manuf Technol 124:1379–1399. https://doi.org/10.1007/s00170-022-10590-9
30. Chung IG, Bolouri A, Kang CG (2012) A study on semisolid processing of A356 aluminum alloy through vacuum-assisted electromagnetic stirring. Int J Adv Manuf Technol 58:237–245. https://doi.org/10.1007/s00170-011-3376-5
31. Kund NK (2018) Effect of tilted plate vibration on solidification and microstructural and mechanical properties of semisolid cast and heat-treated A356 Al alloy. Int J Adv Manuf Technol 97:1617–1626.

https://doi.org/10.1007/s00170-018-2063-1

32. Canyook R, Petsut S, Wisutmethangoon S et al (2010) Evolution of microstructure in semi-solid slurries of rheocast aluminum alloy. Trans Nonferrous Met Soc China (English Ed 20:1649–1655. https://doi.org/10.1016/S1003-6326(09)60353-8
33. Wisutmethangoon S, Thongjan S, Mahathaninwong N et al (2012) Precipitation hardening of A356 Al alloy produced by gas induced semi-solid process. Mater Sci Eng A 532:610–615. https://doi.org/10.1016/j.msea.2011.11.026
34. Chomsaeng N, Haruta M, Chairuangsri T et al (2010) HRTEM and ADF-STEM of precipitates at peak-ageing in cast A356 aluminium alloy. J Alloys Compd 496:478–487. https://doi.org/10.1016/j.jallcom.2010.02.084
35. Samuel AM, Samuel E, Songmene V, Samuel FH (2023) A Review on Porosity Formation in Aluminum-Based Alloys. Mater (Basel) 16. https://doi.org/10.3390/ma16052047
36. Lee CD (2007) Effects of microporosity on tensile properties of A356 aluminum alloy. Mater Sci Eng A 464:249–254. https://doi.org/10.1016/j.msea.2007.01.130
37. Cho WG, Kang CG (2000) Mechanical properties and their microstructure evaluation in the thixoforming process of semi-solid aluminum alloys. J Mater Process Technol 105:269–277. https://doi.org/10.1016/S0924-0136(00)00577-X
38. Kareh KM, Lee PD, Atwood RC et al (2014) Pore behaviour during semi-solid alloy compression: Insights into defect creation under pressure. Scr Mater 89:73–76. https://doi.org/10.1016/j.scriptamat.2014.06.033
39. Ghassemali E, Riestra M, Bogdanoff T et al (2017) Hall-Petch equation in a hypoeutectic Al-Si cast alloy: Grain size vs. secondary dendrite arm spacing. Procedia Eng 207:19–24. https://doi.org/10.1016/j.proeng.2017.10.731
40. Figueiredo RB, Kawasaki M, Langdon TG (2023) Seventy years of Hall-Petch, ninety years of superplasticity and a generalized approach to the effect of grain size on flow stress. Prog Mater Sci 137. https://doi.org/10.1016/j.pmatsci.2023.101131
41. Sebaie O, El, Samuel AM, Samuel FH, Doty HW (2008) The effects of mischmetal, cooling rate and heat treatment on the eutectic Si particle characteristics of A319.1, A356.2 and A413.1 Al-Si casting alloys. Mater Sci Eng A 480:342–355. https://doi.org/10.1016/j.msea.2007.07.039
42. Chen R, Shi YF, Xu QY, Liu BC (2014) Effect of cooling rate on solidification parameters and microstructure of Al-7Si-0.3Mg-0.15Fe alloy. Trans Nonferrous Met Soc China (English Ed 24:1645–1652. https://doi.org/10.1016/S1003-6326(14)63236-2
43. BoChao L, YoungKoo P, HongSheng D (2011) Effects of rheocasting and heat treatment on microstructure and mechanical properties of A356 alloy. Mater Sci Eng A 528:986–995. https://doi.org/10.1016/j.msea.2010.09.059
44. Gebril MA, Omar MZ, Mohamed IF et al (2023) The Microstructural Refinement of the A356 Alloy Using Semi-Solid and Severe Plastic-Deformation Processing. Met (Basel) 13. https://doi.org/10.3390/met13111843

45. Yang B, Song H, Wang S et al (2021) Tension-compression mechanical behavior and corresponding microstructure evolution of cast A356-T6 aluminum alloy. Mater Sci Eng A 821. https://doi.org/10.1016/j.msea.2021.141613
46. Deepak Kumar S, Mandal A, Chakraborty M (2015) On the age hardening behavior of thixoformed A356-5TiB2 in-situ composite. Mater Sci Eng A 636:254–262. https://doi.org/10.1016/j.msea.2015.03.076
47. Haga T, Kapranos P (2002) Billetless simple thixoforming process. J Mater Process Technol 130–131:581–586. https://doi.org/10.1016/S0924-0136(02)00817-8
48. Gu Gchao, Xiang L, xin, Li Rfen et al (2023) Microstructure, segregation and mechanical properties of A356 alloy components fabricated by rheo-HPDC combined with the swirled enthalpy equilibration device (SEED) process. J Mater Res Technol 26:7803–7815. https://doi.org/10.1016/j.jmrt.2023.09.153

Figures

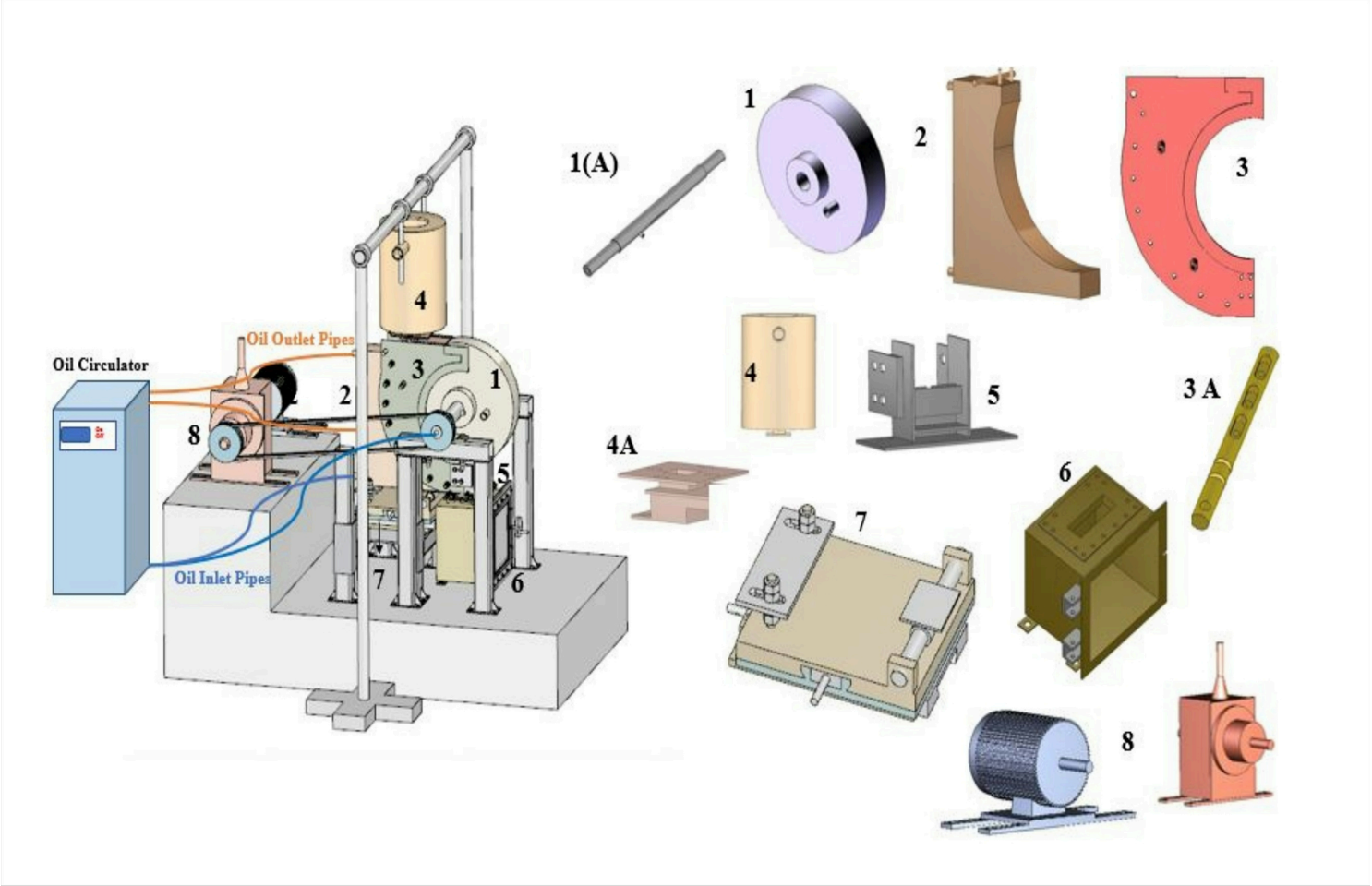


Figure 1

Schematic representation of Modified Shearing Cooling Roll setup (SCR)

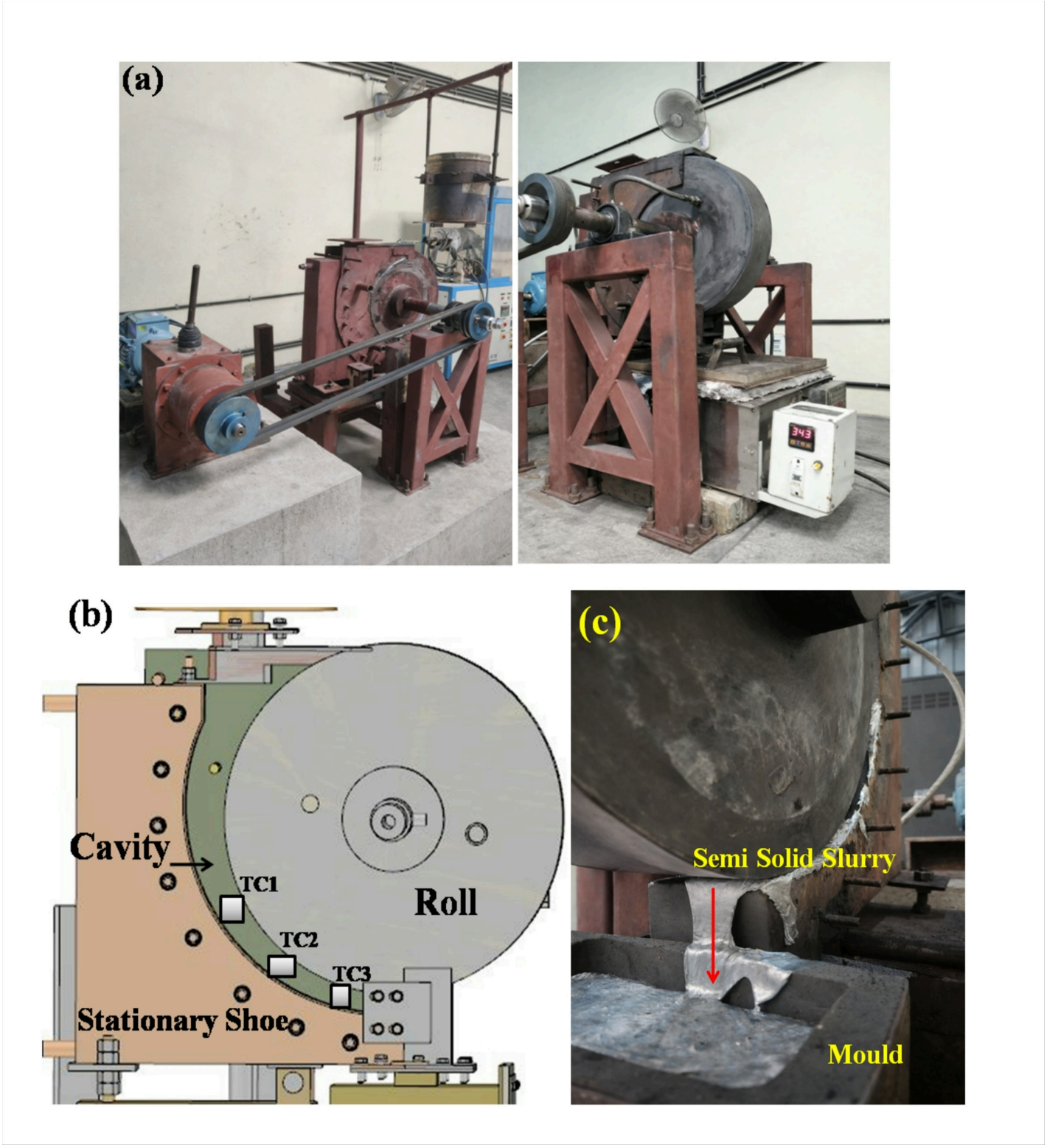


Figure 2

(a) Actual Picture of SCR Setup (b) Side view of the cavity (c) Front view of cavity showing extruded material at the end

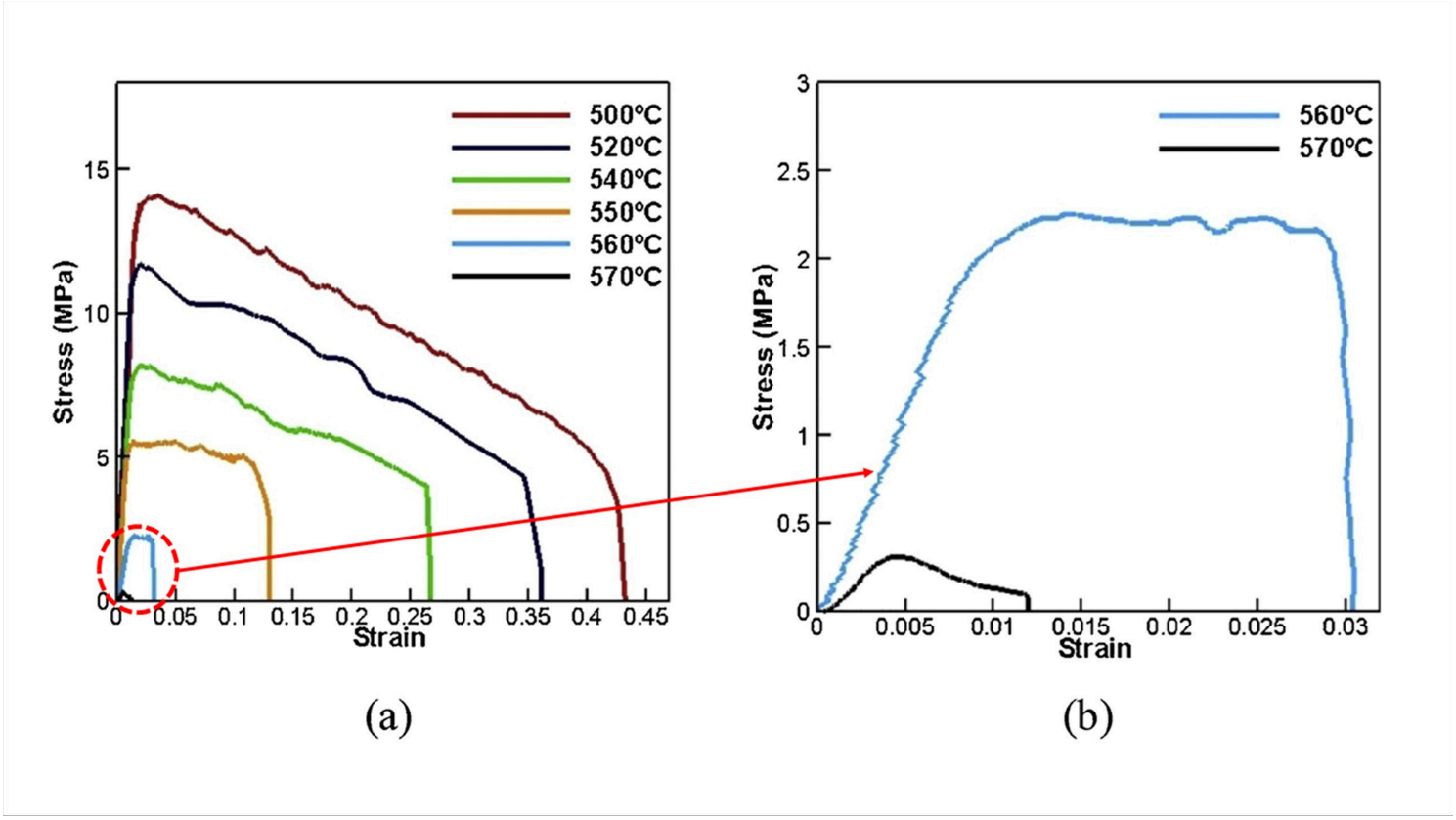


Figure 3

Engineering stress-strain curves of as-cast A356 alloy tested at the temperatures indicated in the legend [24]

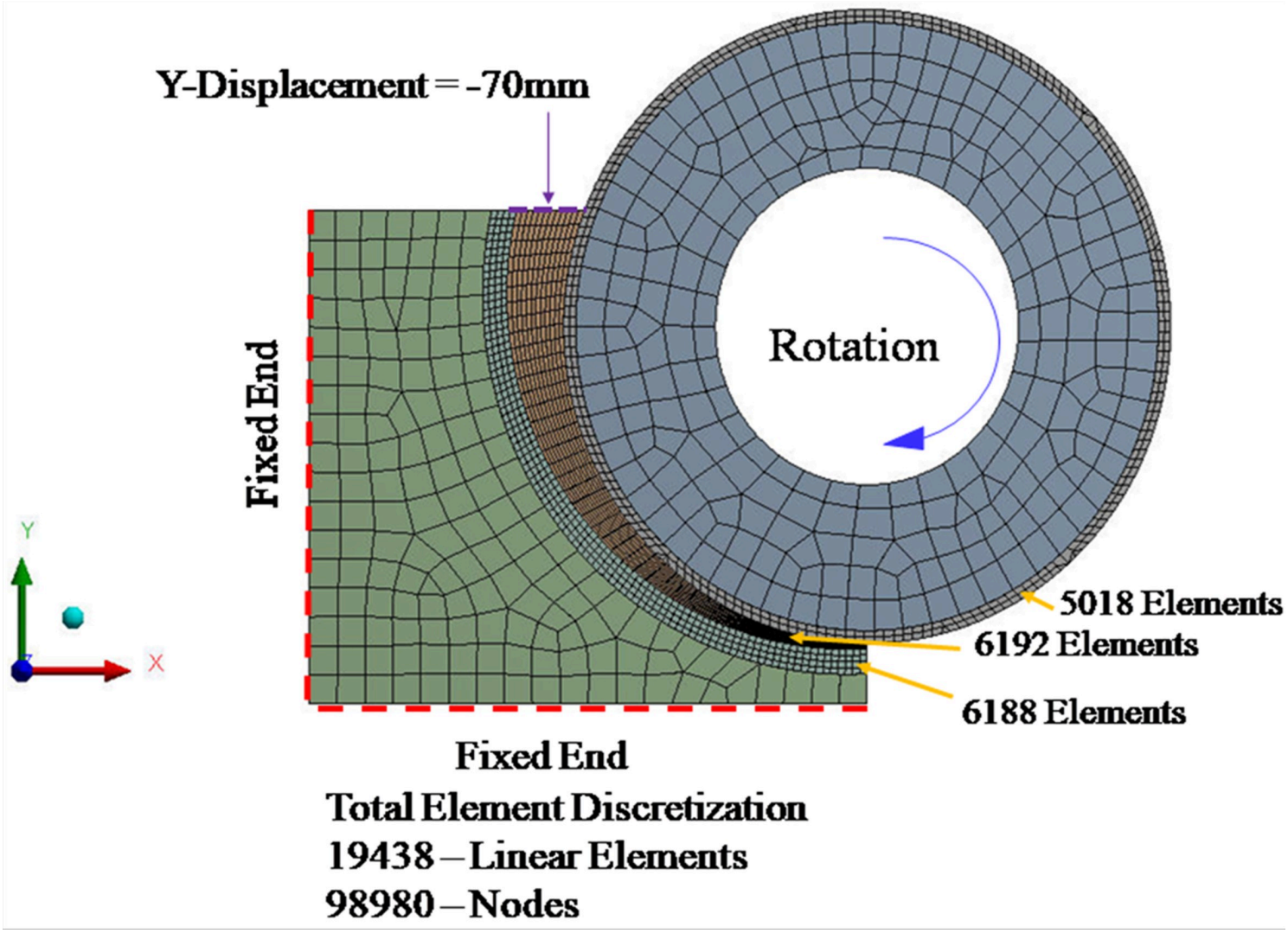


Figure 4

Semi-solid casting mesh showing billet, roll, and support components

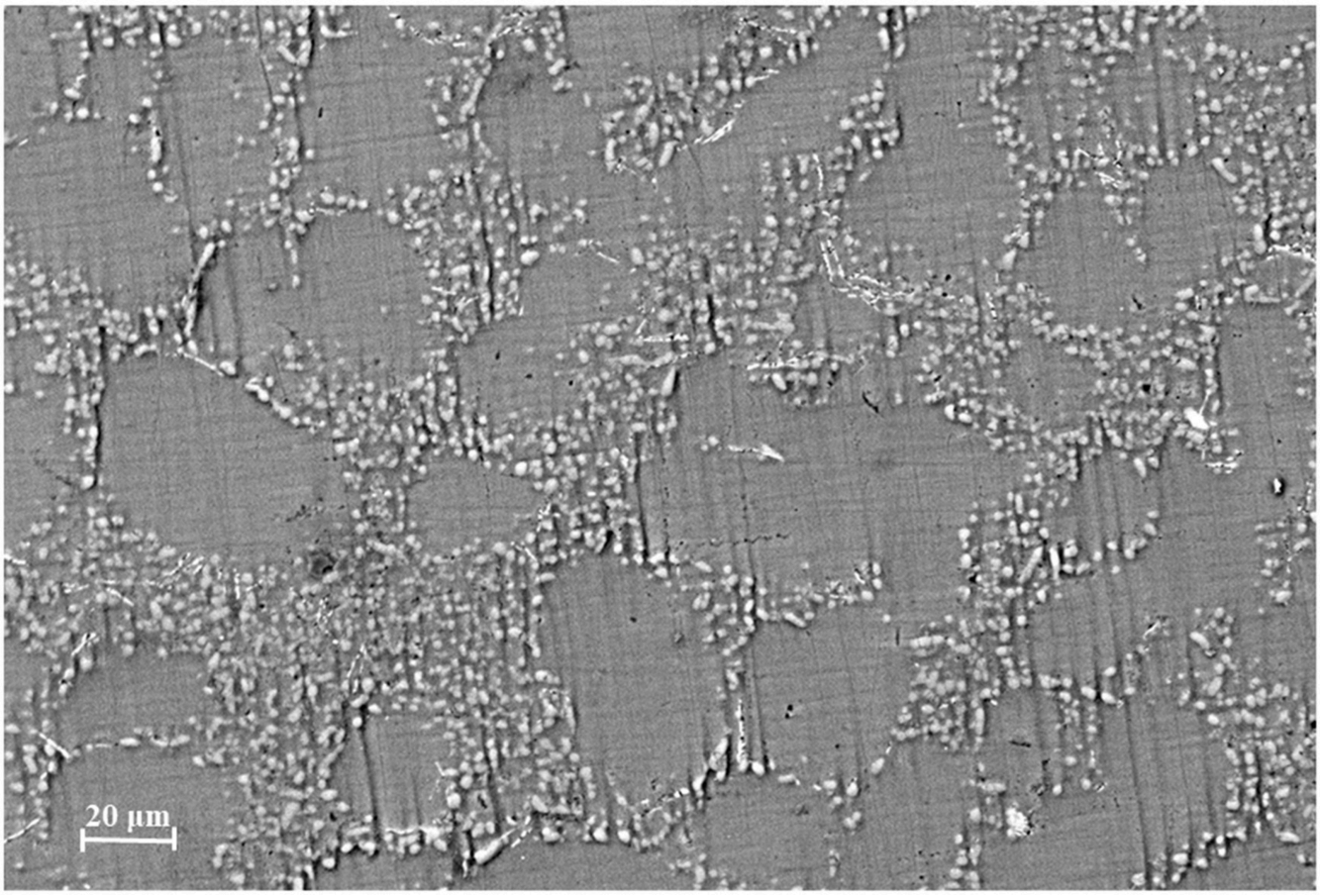


Figure 5

SEM microstructure of eutectic Si morphology in SCR processed A356 alloy

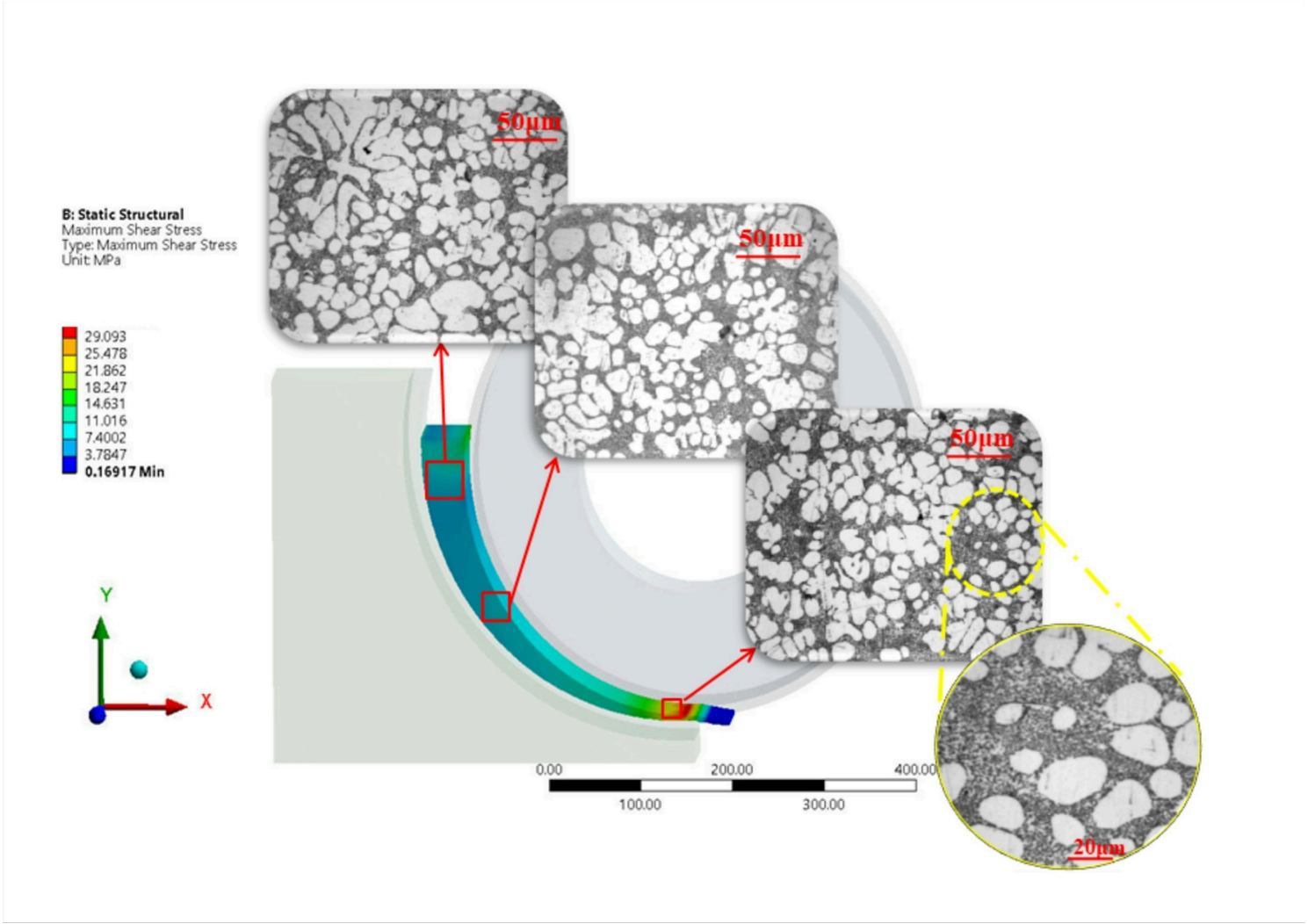


Figure 6

Microstructural evolution across cavity cross-section: (a) Top region, (b) Middle region, (c) Bottom region

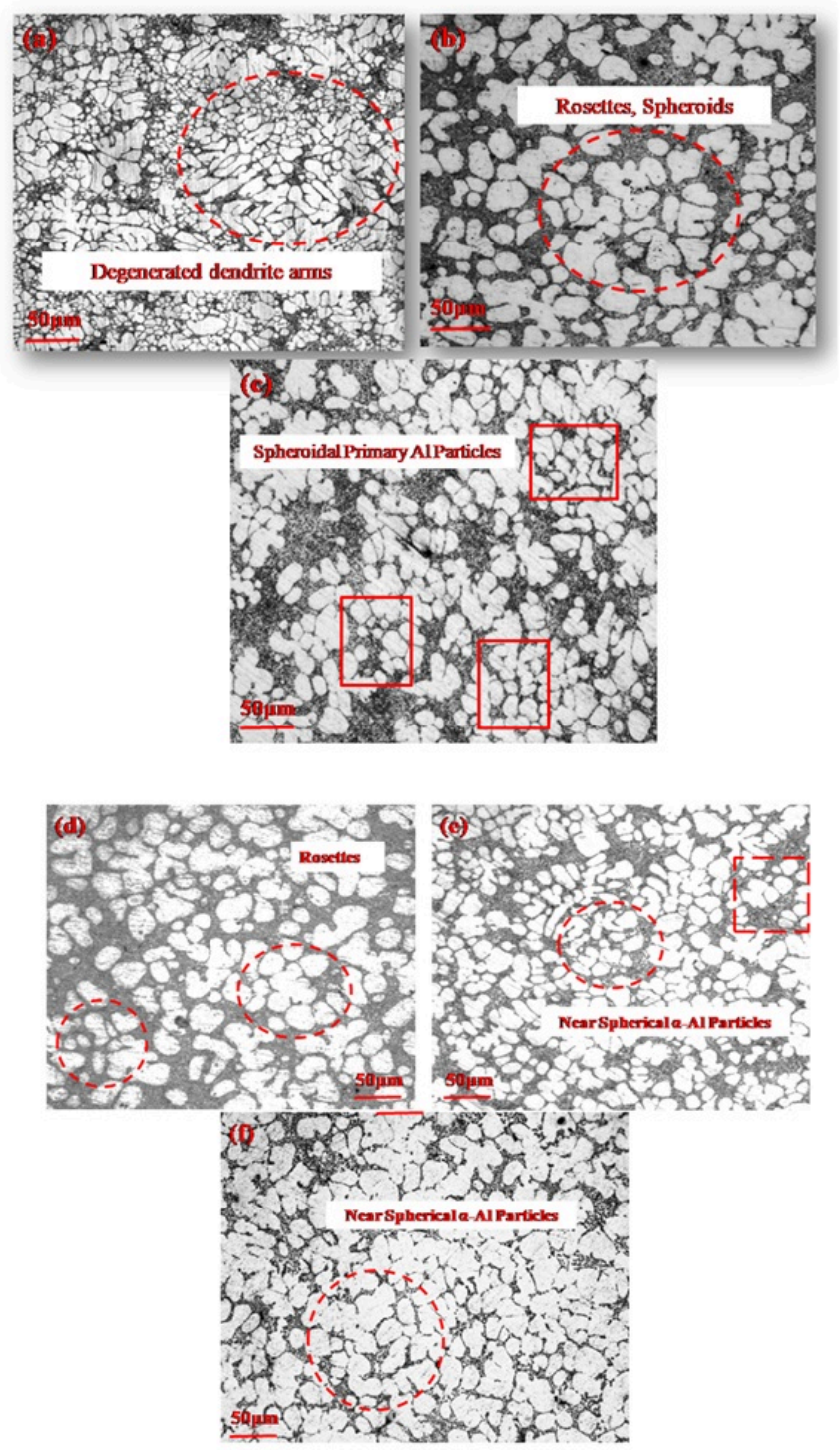


Figure 7

Microstructural evolution of A356 alloy under varying processing conditions: (a–c) Effect of roll speed at constant 6 mm gap - (a) 0 RPM, (b) 40 RPM, (c) 120 RPM; (d–f) Effect of gap size at constant 120 RPM - (d) 8 mm, (e) 6 mm, (f) 4 mm.

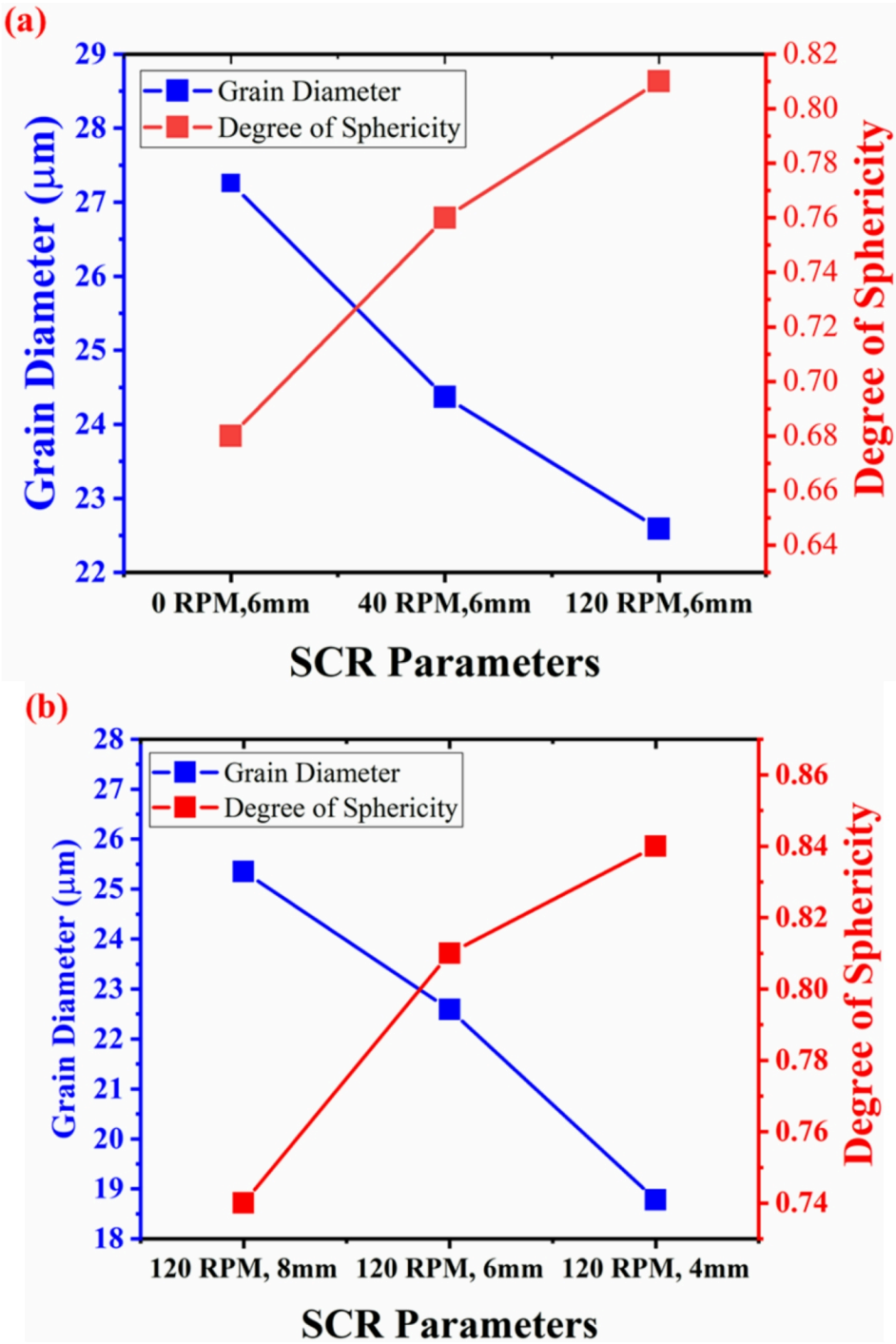


Figure 8

Variation of grain size and DOS with SCR parameters (a) Variation in speed for 6mm gap (b) Variation in gap for 120 RPM speed

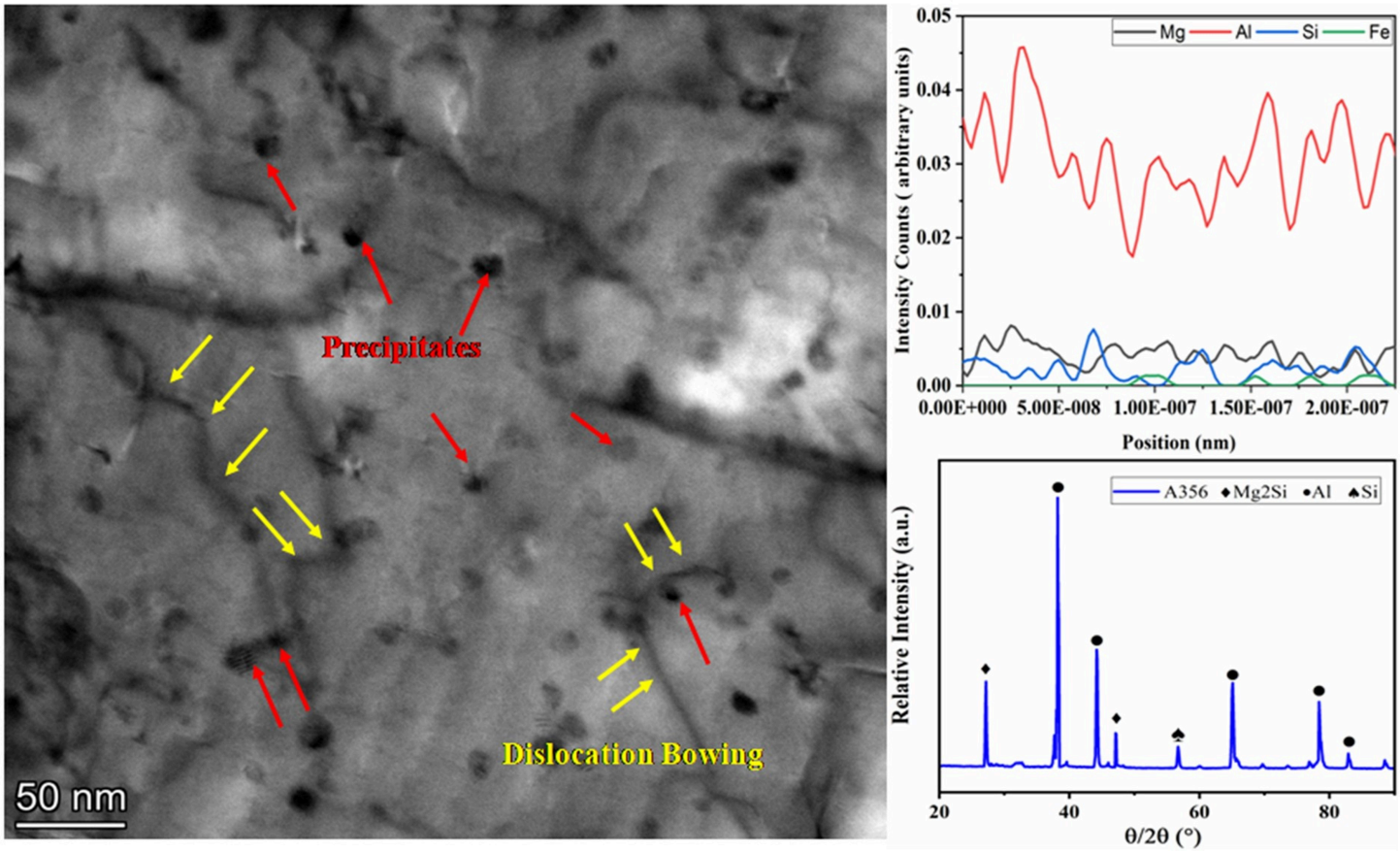


Figure 9

HAADF-STEM, EDS, and XRD analysis of the SCR processed A356 alloy demonstrating refinement of Si phases, precipitation and dislocation interaction

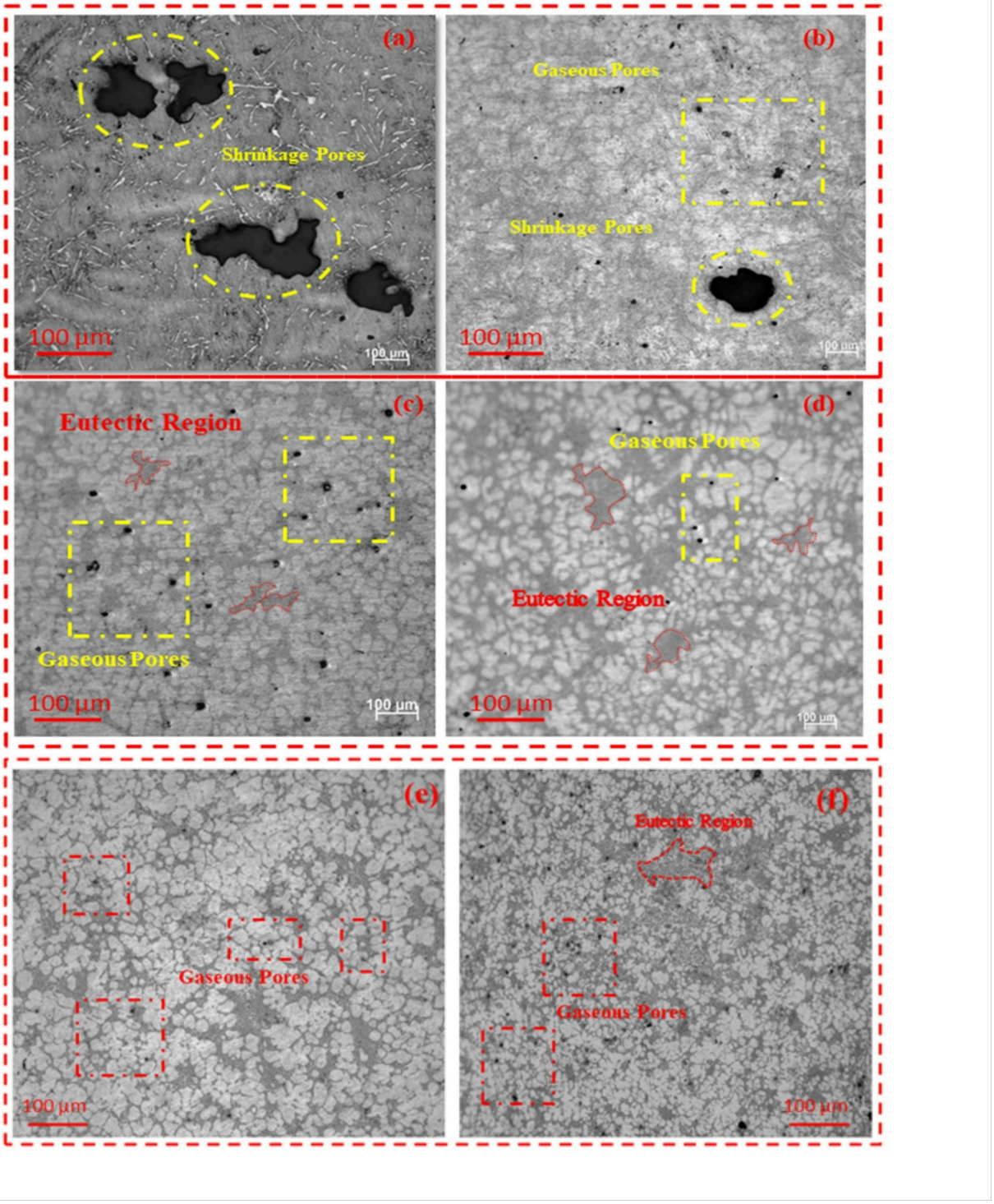


Figure 10

Visualization of shrinkage and gas porosity (a) Gravity Cast (b) 0 RPM, 6mm (c) 40RPM,6mm (d) 120 RPM,8mm (e) 120 RPM,6mm (f)120 RPM,4mm

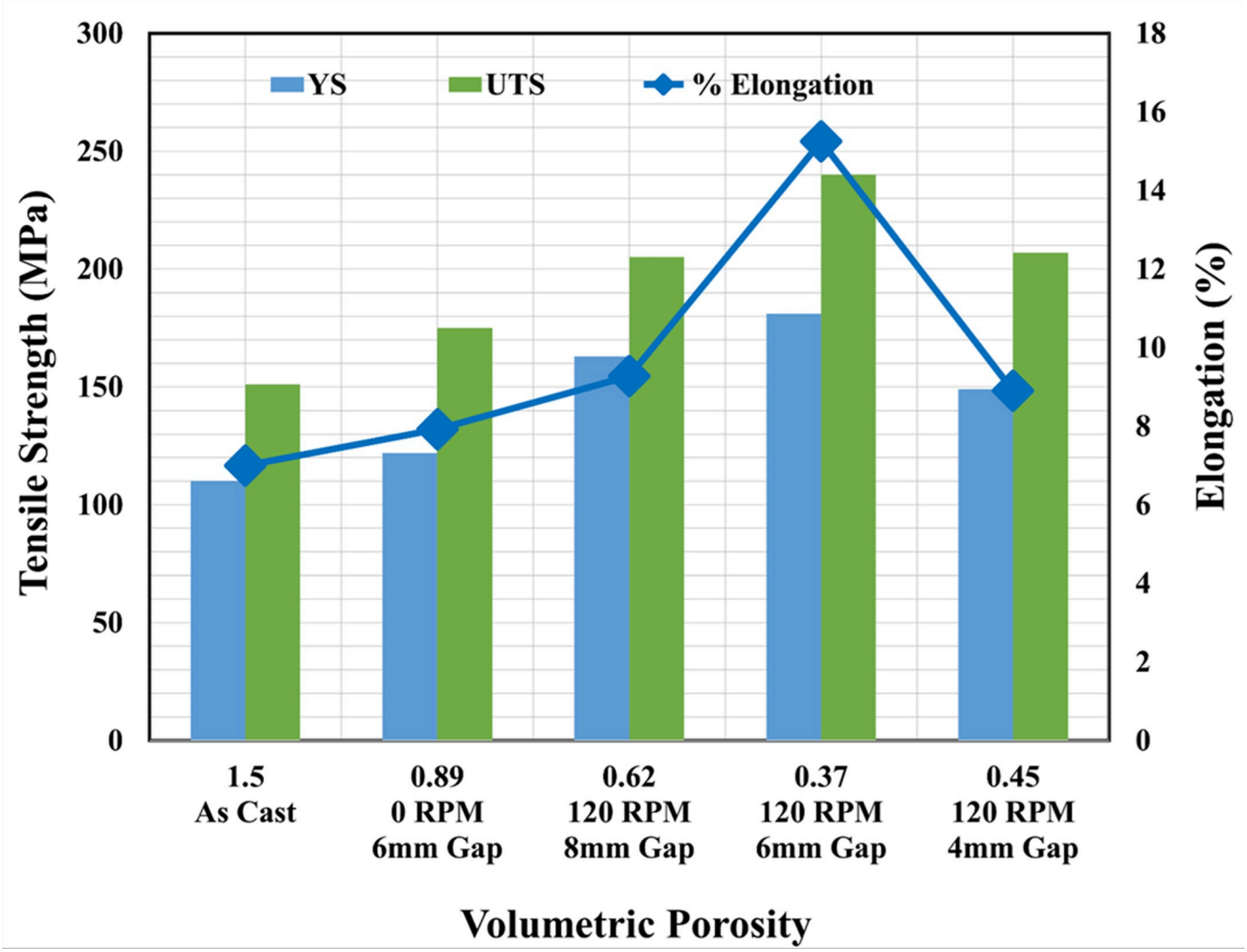


Figure 11

Tensile properties of SCR processed A356 alloy on the microporosity variation

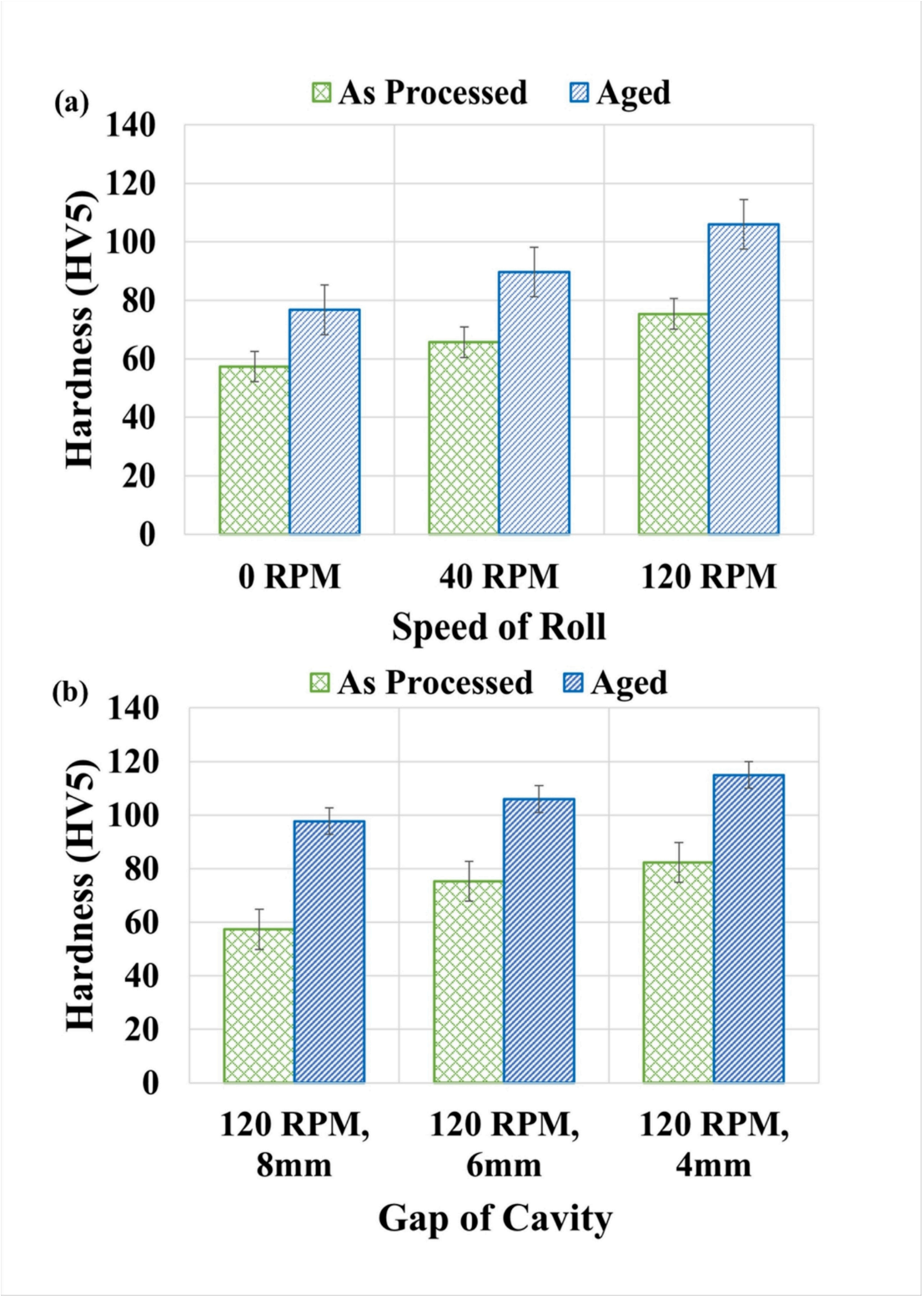


Figure 12

Hardness Variation with SCR Parameters (a) Variation in speed for 6mm gap (b) Variation in gap for 120 RPM speed

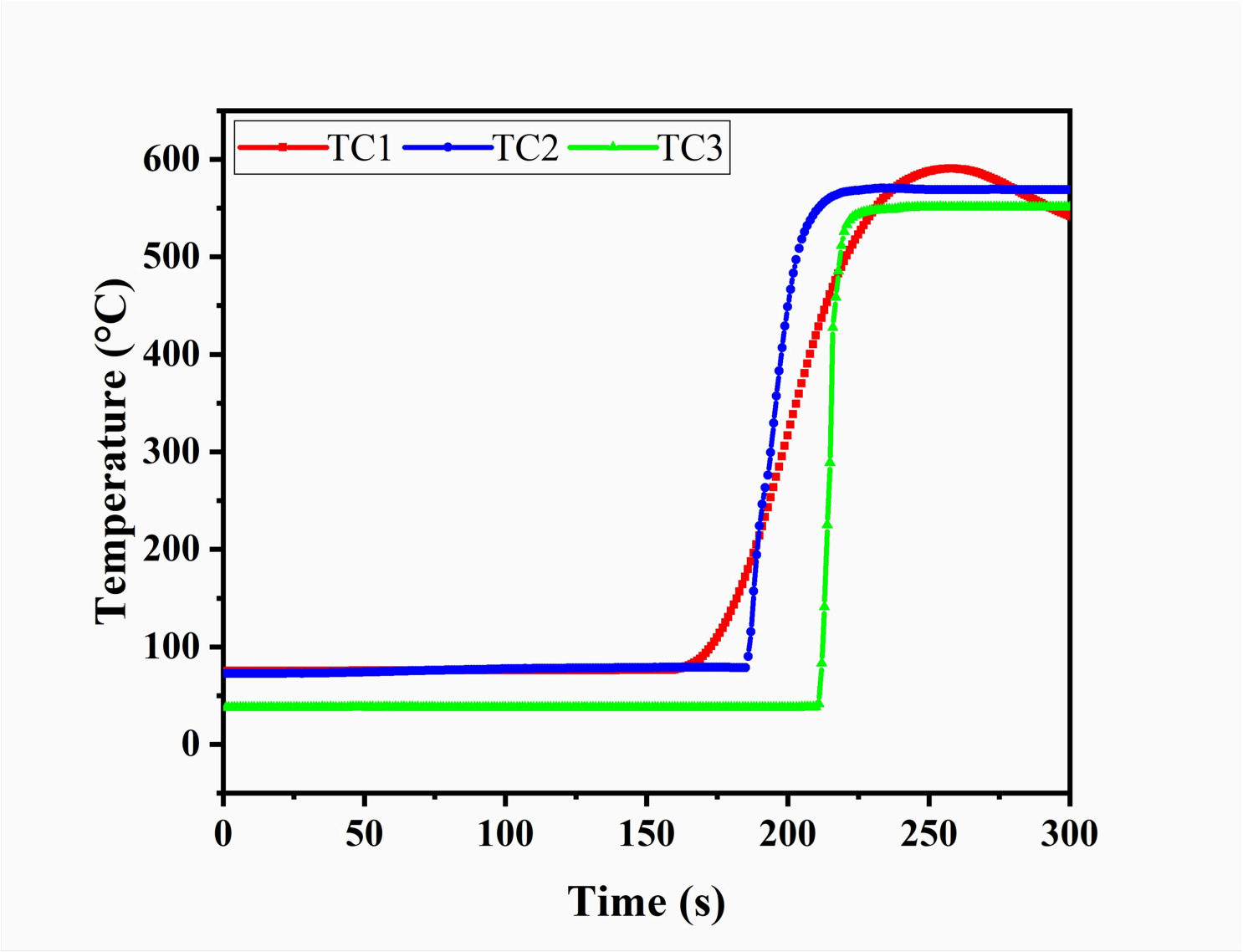


Figure 13

Temperature distribution across the SCR Cavity

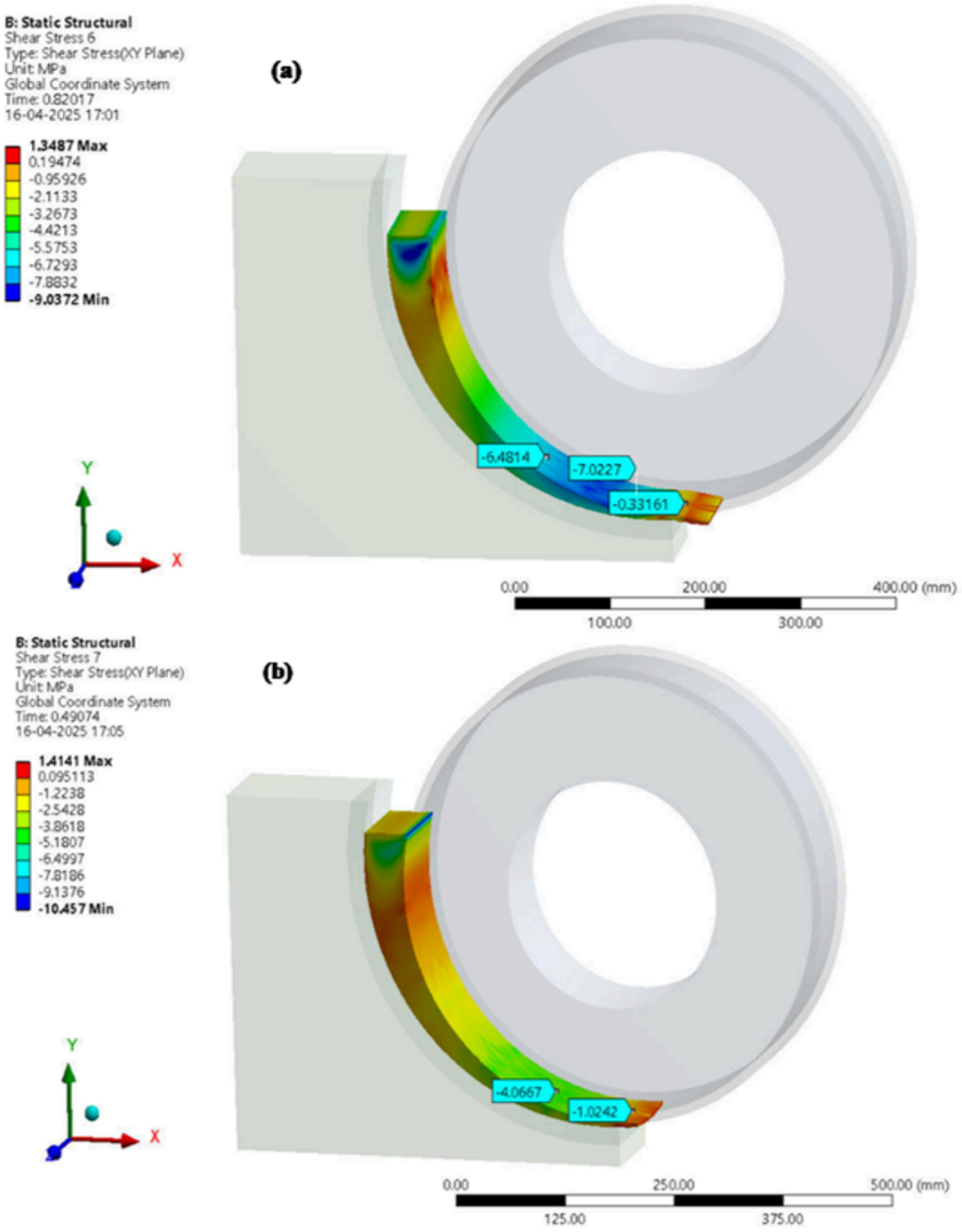


Figure 14

(a) Shear Stress Distribution at 0.82sec, (b) Shear Stress Distribution at 0.49sec

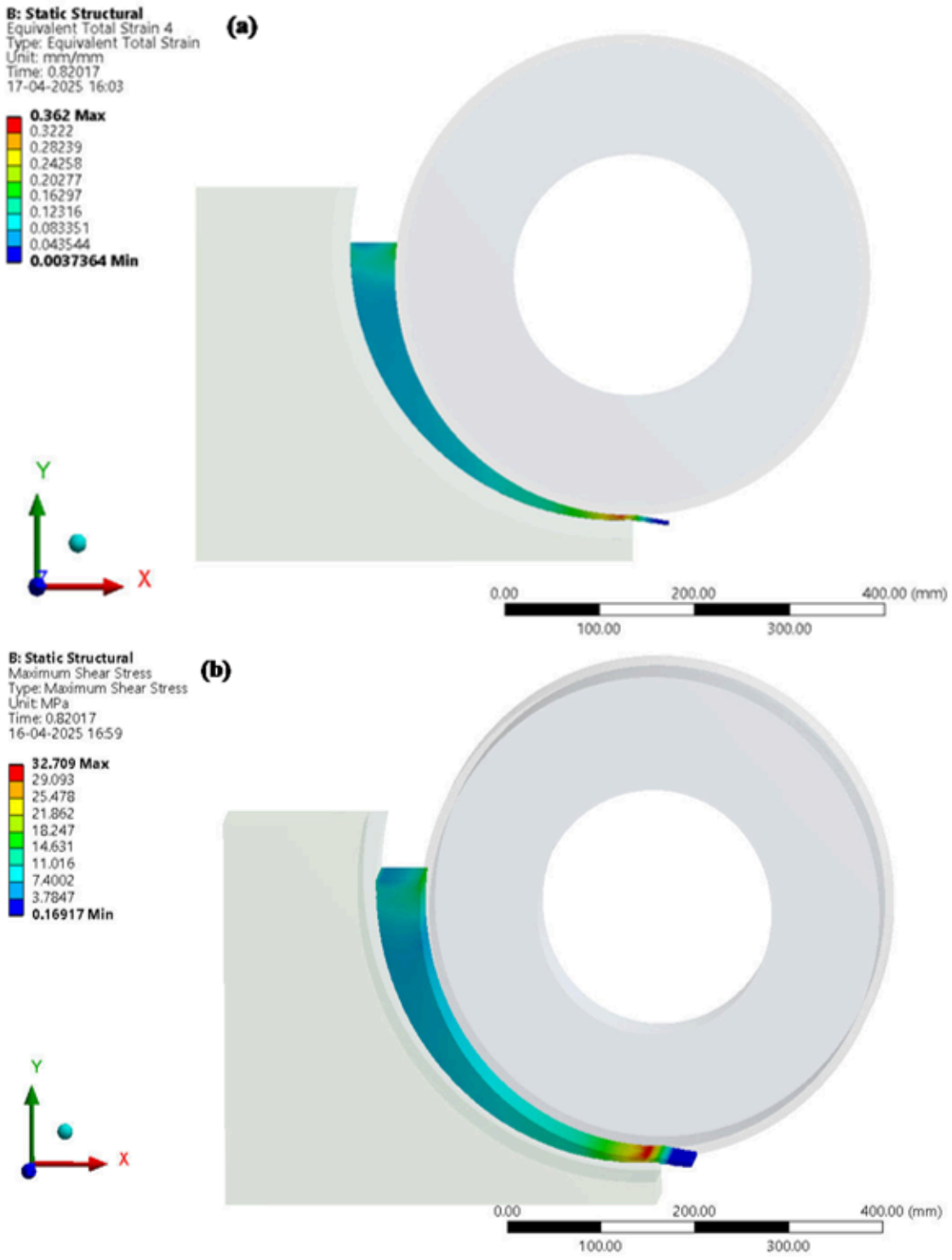


Figure 15

(a) Peak Strain Distribution, (b) Peak Shear Stress Distribution

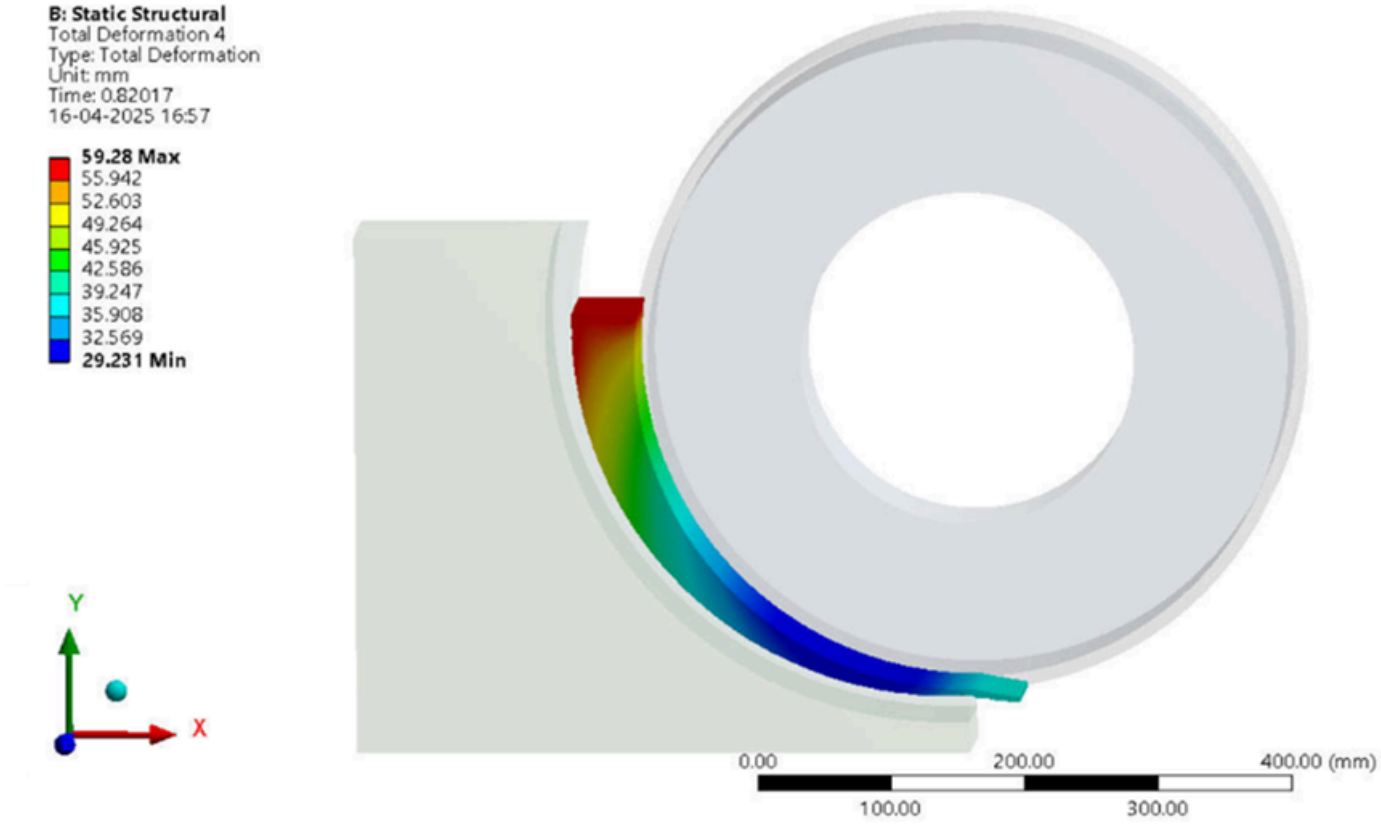


Figure 16

Deformation Behaviour

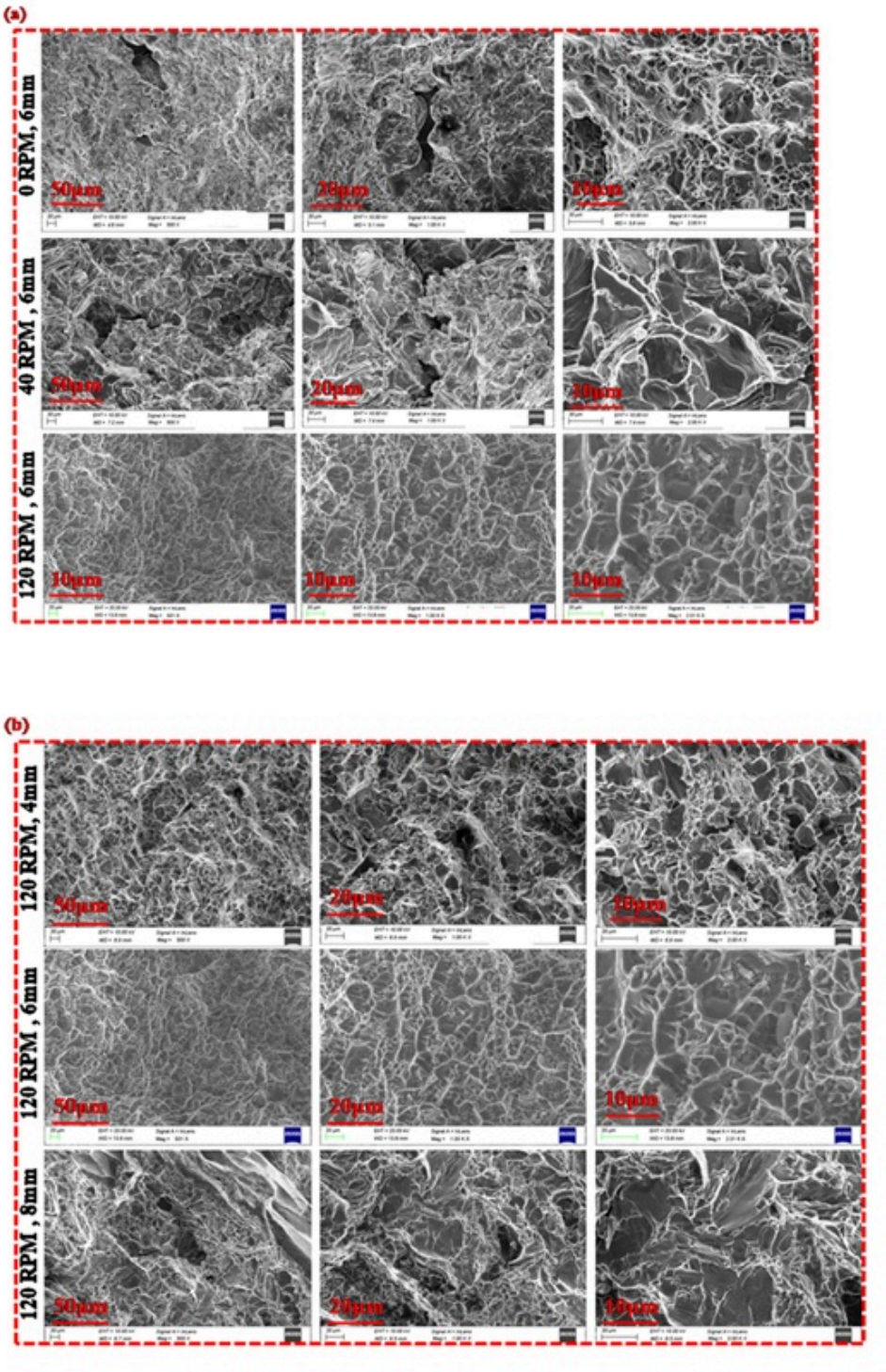


Figure 17

Post tensile fracture features of SCR samples having (a) varying speed and (b) varying gap